

Owl-z: a Bayesian tool to select $z \gtrsim 7$ quasars

M. Ezziati^{1*}, R. Pello¹, J.-G. Cuby^{1,4}, P. Pudlo², F.-X. Dupé³, J.-C. Lambert¹, J.-C. Cuillandre⁵, O. Ilbert¹, S. de la Torre¹, S. Arnouts¹, E. Jullo¹, D. Yang⁶

(Affiliations can be found after the references)

January 15, 2026

ABSTRACT

This paper presents Owl-z, a Bayesian code aiming at identifying $z \geq 7$ quasars in wide field optical and near-infrared surveys. By construction, the code can also be used to select objects that contaminate the high- z quasar population, i.e. brown dwarfs and early-type galaxies at intermediate redshifts. The code can be adapted for the selection of high- z galaxies, and although it has been tuned to the Euclid Wide Survey, it can be easily adapted to other photometric surveys. The code input data are the object's photometric data and its galactic longitude and latitude, and the code output data are the probabilities of the modelled populations of high- z quasars, brown dwarfs and early-type galaxies at intermediate redshift. As part of the validation, Owl-z could re-identify all spectroscopically confirmed quasars at $z \geq 7$, demonstrating the code's versatility in applying to different photometric catalogues. The performance of Owl-z, based on a metric combining completeness and purity called F -measure, is analysed in the case of Euclid using simulated data in a wide range of redshifts ($7 \leq z \leq 12$) and H-band Euclid magnitudes ($18 \leq H_E \leq 24.5$). The results show that Owl-z reaches full performance for bright sources ($H_E \lesssim 22$), somewhat independently of the redshift. We show that the probability threshold used to select promising quasar candidates can be adjusted after processing to fine-tune the F -measure value of candidates depending on their magnitude and redshift estimates. We show that for objects brighter than about two magnitudes above the survey detection limit, Owl-z provides a good classification that will facilitate the optimisation of photometric and spectroscopic confirmation campaigns. In conclusion, Owl-z is a powerful public tool to help select high- z quasars, brown dwarfs or early-type galaxies at intermediate redshifts in Euclid or other wide-field surveys.

Key words. Methods: statistical; Surveys; Cosmology: observations; reionization; quasars: general

1. Introduction

High-redshift quasars are significant in illuminating the early Universe, shedding light on the genesis of initial galaxies and black holes. The luminosity of these cosmic beacons allows for unprecedented insights into the evolution and patchiness of neutral hydrogen and its re-ionization, particularly during the epoch of reionization (EoR; see e.g. [Fan et al. 2006](#); [Becker et al. 2015](#); [Bosman et al. 2022](#)). Beyond tracing the EoR, the identification of supermassive black holes (SMBHs) using quasars at high redshifts challenges conventional models, prompting investigations into alternative scenarios ([Bennett et al. 2024](#)). In particular, the identification and study of $z > 7$ quasars are challenging due to their ambiguous nature and the limited observations/identifications of such objects in the early Universe (see e.g. [Bañados et al. 2018](#); [Fan et al. 2023](#)). Also, the recent discoveries of young quasars with small Lyman-alpha proximity zones ([Übler et al. 2024](#); [Maiolino et al. 2024a](#)) add complexity, opening avenues for refining our understanding of early cosmic phenomena. Spectroscopic observations with the James Webb Space Telescope (JWST) have uncovered Active Galactic Nuclei (AGN) signatures in the spectra of the most distant galaxies known today ([Maiolino et al. 2024b](#)), providing further insights on their environment and formation history ([Scholtz et al. 2024](#)).

Despite their high intrinsic luminosity, high- z quasars appear faint at $z > 7$, and their photometric selection on wide cosmological surveys is particularly challenging. Indeed, their red colours, often used to identify them with the appropriate colour-cuts or photometric redshift estimates, are subject to severe contamination by brown dwarfs and intermediate-redshift galaxies.

With the arrival of massive cosmological surveys, such as Euclid ([Laureijs et al. 2011](#); [Euclid Collaboration et al. 2025](#)), the Nancy Grace Roman Space Telescope ([Akeson et al. 2019](#)) and the Large Synoptic Survey Telescope (LSST; [Ivezic et al. 2019](#)), it becomes possible to identify significant samples of quasars at high redshifts, which will greatly improve our understanding of galaxy and SMBH formation mechanisms. However, for this, it is essential to build efficient and optimised methods and tools. This is precisely the purpose of this work.

The method introduced here, and its associated code Owl-z, is a Bayesian comparison model aiming at optimising the statistical analysis in such a way that the probability of detecting high- z quasars is enhanced with respect to the classical colour-cuts method. Our approach is directly inspired by the Bayesian method developed by [Mortlock et al. 2012](#) and [Euclid Collaboration: Barnett et al. 2019](#) for the search of quasars at high redshifts.

Our method is one of the methods based on Bayesian analysis, along with [Euclid Collaboration: Barnett et al. 2019](#), however, there are other probabilistic methods, such as the one presented in [Nanni et al. 2022](#); [Kang et al. 2024](#), which uses a probabilistic classification approach using density estimation in flux ratio space, specifically using the extreme deconvolution (XD) technique to accurately model the density distribution of high redshift quasar and contaminant populations ([Bovy et al. 2011](#)). There are also other efficient colour-cutting methods paired with radio detections, such as those used in [Belladitta et al. 2020](#), [Bañados et al. 2014](#) and [Bañados et al. 2016a](#), which proved to be very efficient. Last, but not least, there are many recent methods that use Random Forests, a supervised machine learning approach, to effectively select high redshift quasars using

* Corresponding author, e-mail: meriam.ezziati@lam.fr

photometric data from surveys such as Pan-STARRS and WISE (Wenzl et al. 2021).

Owl-z also offers a flexible, fast, and efficient tool for analysing large photometric data sets, looking for $z > 7$ quasars with high performance in terms of completeness and purity of the extracted samples.

From a technical point of view, Owl-z is an open-source code developed specifically for the selection of high- z quasars in wide field near-infrared (NIR) surveys such as the Euclid Wide Survey (hereafter EWS; Euclid Collaboration: Scaramella et al. 2022), but it is adaptable to tackle various other surveys, as also shown in this work.

This paper is organized as follows. In Sect. 2, we present the probabilistic method used for the identification of high- z quasars, the primary objective being the Bayesian selection and classification of each source as either a high- z quasar, an intermediate-redshift contaminant galaxy, or a dwarf star. The detailed modelling performed for each one of these populations is also presented in this section. A brief technical description of Owl-z is presented in Sect. 3. Sect. 4 is devoted to the validation of Owl-z using two different approaches: the successful re-identification of known and spectroscopically-confirmed quasars at $z > 7$ selected from near-IR surveys and simulations of the EWS allowing us to quantify the performance of the code based on the measurement of the completeness and purity of the extracted samples. In Sect. 5, we discuss the influence of several important parameters of the method on the performance of Owl-z, such as the threshold used for the selection of high- z quasars, and we provide some guidelines to optimise their selection and follow-up photometric or spectroscopic campaigns. The summary of conclusions is presented in Sect. 6.

Throughout this paper, the following cosmological parameters have been adopted: $H_0 = 70 \text{ km s}^{-1} \text{ Mpc}^{-1}$, $\Omega_m = 0.3$ and $\Omega_\Lambda = 0.7$. All magnitudes are given in the AB system (Oke & Gunn 1983).

2. Probabilistic selection of sources at high redshift

This section presents the probabilistic selection method for identifying high- z quasars in the EWS. The method can be adapted to other wide-field surveys and to the selection of other high- z astronomical sources. The objective of this method is to identify and select a distinct set of potentially high- z sources, referred to as candidates, by effectively distinguishing them from low-redshift sources designated as contaminants. Our approach is based on the Bayesian method developed by Mortlock et al. 2012 and Euclid Collaboration: Barnett et al. 2019 for the search of quasars at high redshift.

The primary spectral signature of objects with a redshift exceeding 7 ($z > 7$) is the quasi-absence of flux blue-ward the Lyman alpha line, which is a consequence of the combined effects of the Lyman forest and the Gunn-Peterson trough. It is thus possible to identify objects with a redshift of more than 7 by the lack of signal in the optical domain below $\approx 1\mu\text{m}$ (0.97 μm). This allows us to restrict the modelling of high- z quasars and their contaminants to objects detected in near-infrared bands and pre-selected on the basis of the absence or near-absence of detection in optical bands. This work can be compared with others, such as Euclid Collaboration: Barnett et al. 2019 and Pipien et al. 2018b. For details, please see Sect. 5.5

We employ Bayesian selection methodology to ascertain the posterior probability that a specific observed astronomical source, initially identified as non-detected in optical bands, is classified as a high- z quasar or as a contaminant. This is achieved

by considering the prior surface density of the quasars and contaminants. Contaminant populations of high- z galaxies and quasars in near-infrared and mid-infrared bands are well known (see e.g. Mortlock et al. 2012; Euclid Collaboration: Barnett et al. 2019) and consist of early-type galaxies at intermediate redshift ($1 \lesssim z \lesssim 2$, see e.g. Euclid Collaboration: van Mierlo et al. 2022) and low mass dwarf stars of spectral types late-M, L or T (MLT hereafter; Stern et al. 2007; Caballero et al. 2008; Wilkins et al. 2014; Hainline et al. 2024a). The difficulty in distinguishing high- z quasars from the above-mentioned contaminants is illustrated in Fig. 1, showing the comparison of NIR and optical-NIR colours for the three populations considered in this work using Euclid filters (Euclid Collaboration et al. 2022). Analysis of this figure highlights the distinct colour characteristics of these populations in the $Y_E - J_E$ colour space, which is key to the quasar selection process. The top panel of the figure illustrates that at higher redshifts ($z > 8$), quasars are significantly redder than the contaminating populations, allowing for effective separation based on their $Y_E - J_E$ colours. However, the analysis also notes that at lower redshifts ($7 < z < 8$), the NIR broadband colours of quasars and contaminants overlap more, making it difficult to distinguish between them without deep complementary data, especially in the LSST z-band (lower panel).

2.1. Principles

In this section, we present the Bayesian formalism in a general context and then apply it in more detail to each of the populations. Bayesian model selection (Robert 2007) is a relevant method to establish the nature of a source in a survey given photometric data (see Mortlock et al. 2012, and the references therein). The posterior probability that a given source is of a type $t \in \mathcal{T}$, given the data \mathbf{D} , is driven by two terms: the prior probability $\mathbb{P}(t)$ of the source being of type t , and the integrated likelihood or the evidence of the data given the type of source, $\mathbb{P}(\mathbf{D}|t)$. The latter is the marginal likelihood of the data, which is the integral of the likelihood of the data given the parameters of the model, $\mathbb{P}(\mathbf{D}|\theta_t, t)$, with respect to the prior distribution of the parameters, $\mathbb{P}(\theta_t|t)$. The marginal likelihood is the key quantity in Bayesian model selection: Unlike methods based on best-fit parameters and type, it accounts for the diversity of photometric data of a given type. The posterior probability of a source being of type t is then given by Bayes' theorem:

$$\mathbb{P}(t|\mathbf{D}) = \frac{W(t|\mathbf{D})}{\sum_{t' \in \mathcal{T}} W(t'|\mathbf{D})}, \quad (1)$$

where $W(t|\mathbf{D}) = \mathbb{P}(t)\mathbb{P}(\mathbf{D}|t)$ is the weighted evidence of the model t given the data \mathbf{D} . The weighted evidence of type t is given by

$$W(t|\mathbf{D}) = \mathbb{P}(t)\mathbb{P}(\mathbf{D}|t) = \mathbb{P}(t) \int \mathbb{P}(\theta_t|t)\mathbb{P}(\mathbf{D}|\theta_t, t)d\theta_t \\ = \int \rho_t(\theta_t)\mathbb{P}(\mathbf{D}|\theta_t, t)d\theta_t, \quad (2)$$

where θ_t is the vector of parameters of t -type object and $\rho_t(\theta_t)$ is the prior value of surface density of detected objects of type t and parameters θ_t in the sky. A photometric dataset is a set $\widehat{\mathbf{F}} = (\widehat{F}_1, \dots, \widehat{F}_N)$ of N measurements of the flux of a source in N photometric bands, and their standard error $\widehat{\sigma} = (\widehat{\sigma}_1, \dots, \widehat{\sigma}_N)$. The statistical model of each type of source is built on a set of spectral energy densities (SEDs) of n_t templates. Given the i -th SED of type t , we can compute expected fluxes in each band, $\mathbf{F}_{t,i}(\theta_t) = (F_{t,i,1}(\theta_t), \dots, F_{t,i,N}(\theta_t))$ at value θ_t of the parameter.

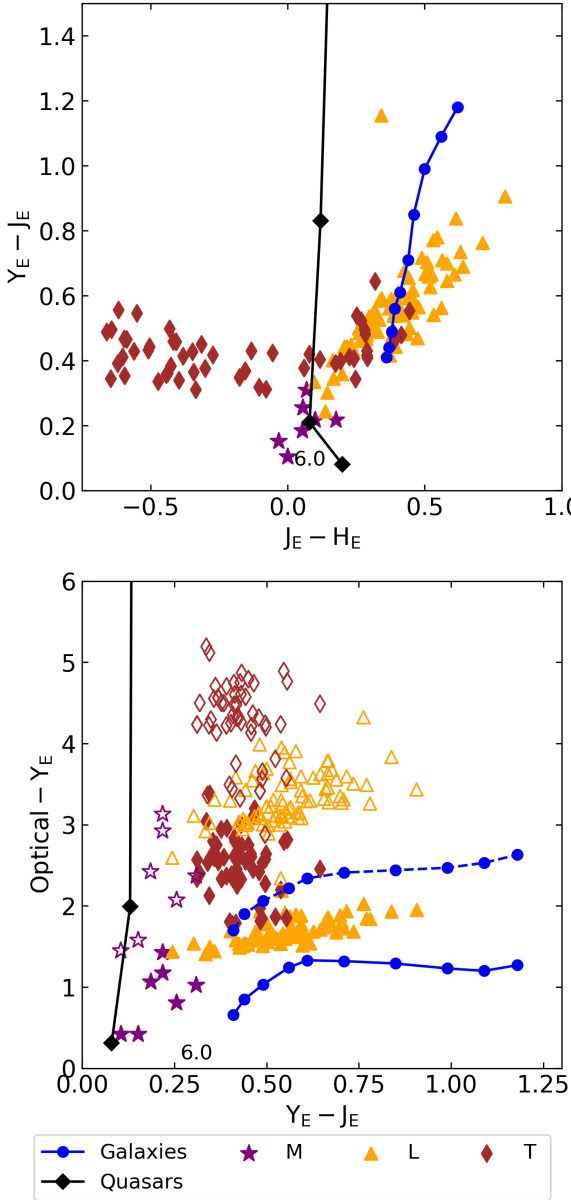


Fig. 1: NIR (top) and Optical-NIR (bottom) colours for the three classes of objects considered in this work, using Euclid filters. Black solid lines display quasars in the redshift domains captured by the filters, with redshifts indicated directly on the lines. Blue lines display galaxies at $(1 \leq z \leq 2)$, susceptible to contaminating the quasar samples. MLT: stars M, triangles L, and diamonds T. For the M, L and T, filled: $z - Y_E$ and hollow: $I_E - Y_E$

The likelihood of the data given θ_t and t is set as the mixture of multivariate densities is given by

$$p(\widehat{\mathbf{F}}|\theta_t, t) \sim \frac{1}{n_t} \sum_{i=1}^{n_t} p(\widehat{\mathbf{F}}|\mathbf{F}_{t,i}(\theta_t), \widehat{\sigma}), \quad (3)$$

centred at $\mathbf{F}_{t,i}(\theta_t)$ and with dispersion given by $\widehat{\sigma}$.

The above mixture sets a uniform prior distribution on the SED templates modelling each population. If the photometric bands do not overlap, we can neglect the correlation between the fluxes in different bands. Thus, we rely on a product of Gaussian distributions truncated to be non-negative, given by

$$p(\widehat{\mathbf{F}}|\mathbf{F}_{t,i}(\theta_t), \widehat{\sigma}) = \prod_{j=1}^N \mathcal{L}_j, \quad (4)$$

where each truncated Gaussian distribution is given by

$$\mathcal{L}_j = \frac{\exp\left(-\frac{1}{2}\left(\frac{\widehat{F}_j - F_{t,i,j}(\theta_t)}{\widehat{\sigma}_j}\right)^2\right)}{\widehat{\sigma}_j \sqrt{2\pi} \left(1 - \mathcal{N}\left(-\frac{F_{t,i,j}(\theta_t)}{\widehat{\sigma}_j}\right)\right)}, \quad (5)$$

where $\mathbb{I}_{\widehat{F}_j \geq 0}$ is the indicator function that the flux is non-negative and \mathcal{N} is the cumulative distribution function of the standard normal distribution given by

$$\mathcal{N}(z) = \frac{1}{2} + \frac{1}{2} \operatorname{erf}\left(\frac{z}{\sqrt{2}}\right).$$

Note that the χ^2 -criterion that is used to produce the best-fit parameters in the frequentist approach appears in the exponent of the likelihood given in Eq. (5).

In a general context, faint sources are measured with a low signal-to-noise ratio (SNR) in one or more bands. Forced photometry is a practice that is applied in many surveys, including Euclid, using detected images from which aperture fluxes are measured for all undetected sources. The likelihood is then calculated using Eq. (5) even when the forced photometry flux has a negative or null value. However, when this is impossible i.e. there is no estimation of the flux in a certain band, we re-write the likelihood with an unknown measured flux. This allows us to calculate the probability that a source is observed with a measured flux below the stated detection limit. This probability can be expressed as follows:

$$\mathcal{L}_j = \frac{\mathcal{N}\left(\frac{\widehat{F}_{lim} - F_{t,i,j}(\theta_t)}{\sqrt{\widehat{\sigma}_j}}\right)}{1 - \mathcal{N}\left(-\frac{F_{t,i,j}(\theta_t)}{\widehat{\sigma}_j}\right)}. \quad (6)$$

In Owl-z, Eq. (2) is calculated in two separate steps: initially to build a model and subsequently during comparison of the model with the sources' photometry.

For each population, Owl-z calculates the colours in all bands to build a model by generating maps of the values of colour for each population for each parameter value. The SED and the desired ranges of the parameters are used. Subsequently, the colours are calculated through the integration of magnitudes, as outlined by Hogg et al. 2002, across all SEDs employed. The model comparison step is located within the central portion of the code, where Owl-z examines each candidate for which comprehensive photometry is available (including associated errors), and contrasted it with the models. For each parameter set, it compares the photometry to all model fluxes. The model fluxes are calculated using the colours and model reference magnitude that we choose to be the H band in this work. However, any reference magnitude could be selected, provided that a detection is made in this band. It should be noted that Owl-z does not calculate the probability from the best value of the weighted evidence but rather from the integration of all values. Subsequently, the probability for each population is calculated using Bayes probability

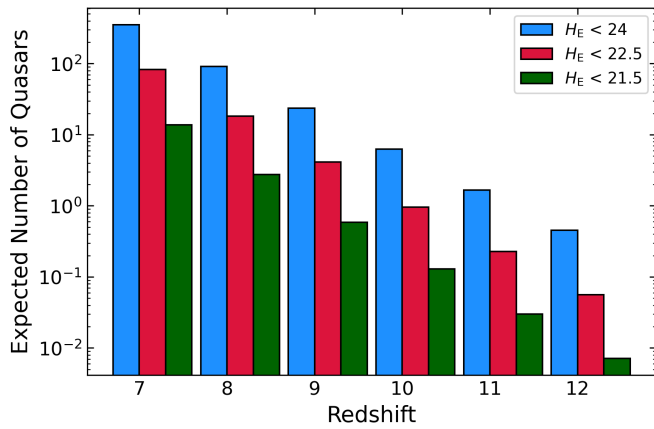


Fig. 2: The expected number of quasars per redshift bin in the 15,000 deg² EWS given the high- z quasar Luminosity Function adopted in this paper. In blue are shown the numbers of quasars expected up to $H_E < 24$, in crimson with $H_E < 22.5$ and in green with $H_E < 21.5$

in Eq. (1). In addition, Owl-z incorporates snippets of code that facilitate the recovery of parameters enabling the calculation of the maximum a posteriori, thus providing the best-fit parameters for a given candidate (see Sec. 3.2).

2.2. The high- z quasars population

The statistical model of the quasar (QSO) population is based on a collection n_{QSO} of SEDs (also referred to as spectral templates or templates) and a set of parameters θ_{QSO} describing the quasars' properties. The spectral templates used in this paper are smoothed versions of the quasar composites presented in Bañados et al. 2016b and parametric SED models that accurately reproduce the observed optical and NIR colours of luminous Type 1 quasars over a wide range of redshifts and luminosities from Temple et al. 2021. The parameters are the redshift z and the apparent magnitude in a reference band, which we choose to be the Euclid H band, denoted H_E . This allows us to compute the expected fluxes in each band, $F_{\text{QSO},i}(\theta_{\text{QSO}})$ at the $\theta_{\text{QSO}} = (H_E, z)$ value of the parameter set given the i -th SED model. The QSO likelihood of the data given θ_{QSO} is defined as the mixture of multivariate densities in Eq. (3). For the purposes of our paper, we let the redshift vary in the range $7 \leq z \leq 12$. We aim for a maximum redshift of 12 as the Euclid bands will cover up to the H_E band, and the Lyman-alpha emission line stays in the J_E band until $z \approx 12$.

To characterise the prior distribution of high- z quasars, we adopt the double power law parametric Luminosity Function (LF) from Willott et al. (2010) and adjust the parameters fit to Matsuoka et al. 2023:

$$\Phi(M_{1450}, z) = \frac{10^{k(z-7)} \Phi^*}{10^{0.4(\alpha+1)(M_{1450} - M_{1450}^*)} + 10^{0.4(\beta+1)(M_{1450} - M_{1450}^*)}}, \quad (7)$$

where M_{1450} is the quasar rest-frame absolute magnitude at $\lambda = 1450\text{\AA}$ and $\Phi(M_{1450}, z)$ is the number of quasars per magnitude bin, and unit volume at redshift z . The parameters are the normalisation Φ^* , the break magnitude M_{1450}^* , the bright end slope β and the faint end slope α , their values can be found in Table 1. Using the apparent magnitude in the H_E band, we can

write the surface density of quasars in the sky in mag⁻¹ × deg⁻² × dz⁻¹ units as:

$$\rho_{\text{QSO}}(H_E, z) = \frac{1}{4\pi} \times \frac{dV_c}{dz} \times \Phi [H_E - \mu - K_{\text{corr}}(z), z], \quad (8)$$

where

– μ represents the distance modulus, defined as a function of the luminosity distance D_L by

$$\mu = \frac{5 \log_{10}(D_L/10 \text{ pc})}{\text{pc}}, \quad (9)$$

– $K_{\text{corr}}(z)$ denotes the K-correction, which converts the absolute magnitude at rest-frame $\lambda = 1450\text{\AA}$ into the observed H -band magnitude, and

– $\frac{1}{4\pi} \times \frac{dV_c}{dz}$ is the co-moving volume element per steradian and per redshift interval dz .

Fig. 2 illustrates the number of quasars per redshift bin and up to three different values of H_E across the entire 15,000 deg² of the EWS, as derived from Eq. (8). This demonstrates that Euclid will detect tens of quasars brighter than $H_E \approx 22.5$ between redshifts 7 and 8, and potentially a few up to $z \approx 9$. Up to this H_E magnitude, the selection with Owl-z will be robust while becoming increasingly more hazardous beyond it.

Table 1: Quasar Luminosity function parameters

α	β	k	M_{1450}^*	$\phi^* 10^{-8} (\text{Mpc}^{-3} \text{mag}^{-1})$
-1.2	-3.34	-0.47	-24.38	0.475

2.3. The MLT stars population

For the purpose of our Bayesian analysis, we need to model the spatial distribution of MLT dwarfs, their luminosity, and spectral energy distributions from the optical to the near-infrared. For spectral energy distributions, we use the stellar dwarf Luyten Half-Second (LHS) library (Bakos et al. 2002) for M3-M5 brown dwarfs and the brown dwarf spectral library SpeX prism (Burgasser 2014; Burgasser & Splat Development Team 2017) for other spectral types. The use of spectral data enables magnitudes and colours to be correctly determined and modelled in the Euclid filters or any other filters as long as they overlap the spectral range of the spectra. Moreover, there are between 5 and ≈ 50 spectra available for each spectral type. Our models also include WISE photometric data for the W1 and W2 bands, anchored to the average JHK photometry of brown dwarfs as tabulated in Best et al. 2017. This allows us to include in our model the WISE photometry that cannot be calculated from the MLT spectra that do not extend beyond the K band. Fig. 3 shows the W1 – W2 colours for all MLT types as indicated in Best et al. 2017, showing that T dwarfs, especially late types, have very strong W1 – W2 colours that can easily be discriminated from the colours of high- z quasars.

To estimate the probability of brown dwarf contamination when searching for high redshift objects in wide-field imaging datasets, the spatial distribution of stellar dwarfs in the Galaxy is usually modelled and restricted to the thin disk of the Milky Way (Caballero et al. 2008; Euclid Collaboration: Barnett et al.

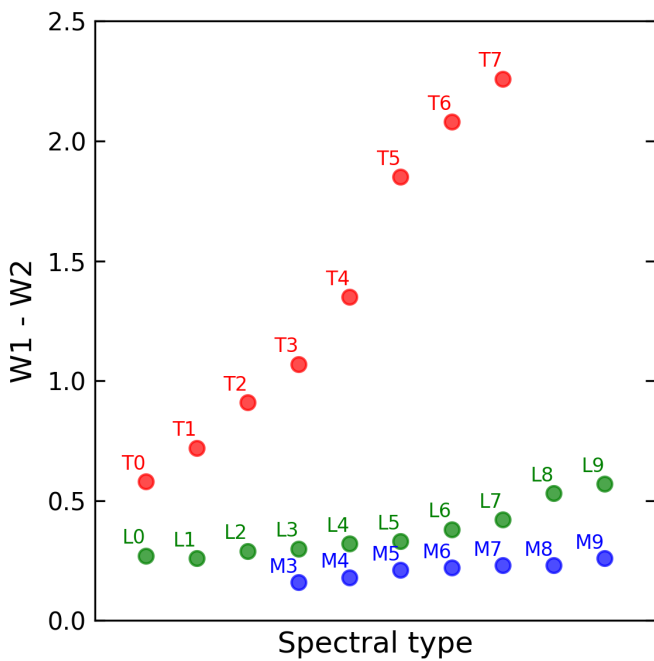


Fig. 3: WISE $W_1 - W_2$ colours of MLT dwarfs from Best et al. 2017 shown in blue, green, and red, respectively, with the values indicating their spectral type.

2019; Pipien et al. 2018b). Detailed modelling of the thin disk is beyond the scope of this paper, and we therefore follow Caballero et al. 2008 by assuming a similar thin-disk scale height for LT dwarfs to its value determined from earlier stellar dwarf types (GKM) and a simplified exponential vertical and horizontal distribution. For detailed theoretical modelling of thin disk parameters as a function of stellar age and metallicity, calibrated against Gaia and APOGEE data, see, for example, Sysliatina, K. & Just, A. 2022.

At the magnitudes corresponding to the depth of the EWS (~ 24), the distance to T dwarfs varies from ~ 150 pc for the coldest to ~ 450 pc for the hottest. With a scale height of the thin disk of the order of 300 pc (Gaia Collaboration et al. 2023; Vieira et al. 2022), we infer that the sole thin disk approximation will reasonably well represent the population of T dwarfs detectable in the EWS. However, the same will not be true for M dwarfs. An M6 dwarf at an apparent magnitude $H_E \approx 24$ is at a distance of ~ 4000 pc, extending well beyond the thin disk into the thick disk or the halo. As a matter of fact, the James Webb Space Telescope has revealed in extragalactic fields a significant number of extremely faint and low-temperature brown dwarfs extending well into the thick disk and possibly into the halo, at distances of up to 2 kpc (Hainline et al. 2024b,a; Burgasser et al. 2024). An analysis of the thick disk contamination is therefore warranted.

For this analysis, we follow a similar approach to that used in Ryan & Reid 2016 and compare the distribution of stellar dwarfs in thin and thick disks as a function of magnitude. We adopt a value of 330 pc for the scale height of the thin disk (Caballero et al. 2008), 800 pc for the scale height of the thick disk (Vieira et al. 2023), 2250 pc (Caballero et al. 2008) for the value of the scale length of both disks and a normalisation factor between the thick and thin disks local densities of 10%. Using Eq. (12) of Pipien et al. 2018b, we compare brown dwarf densities for different spectral types in the thin and thick disks for two lines of

sight: $b = 90^\circ$ and $(l, b) = (90^\circ, 30^\circ)$ (the lowest Galactic latitude of the EWS is $b = 23^\circ$). For local volume densities in the Galactic plane and absolute Euclid magnitudes by spectral type, we refer to Table 2 of Euclid Collaboration: Barnett et al. 2019 and the references therein (Dupuy & Liu 2012; Skrzypek et al. 2016; Bochanski et al. 2010). Late-type M dwarfs can potentially contaminate searches for galaxies or quasars at high redshift in some surveys, whereas, as we will see later, only L and T-type brown dwarfs contaminate the search for $z \geq 7$ with Euclid. Consequently, for the purposes of this paper, we restrict our analysis to the brown dwarf population within the M dwarf population, that is, dwarfs of a type later than approximately M6.

The analysis (see Fig. 4) indicates that up to Euclid magnitude $H_E \sim 24$, the thin disk dominates the number of L and T dwarfs at low and high Galactic latitudes. For M6 to M9 dwarfs, the thick disk is the main contributor above $H \sim 22.5$ magnitudes at high Galactic latitudes, whereas at low Galactic latitudes, the thin disk dominates up to $H_E \sim 24.5$ and beyond. For the purposes of our paper, Galactic latitude is, therefore, the dominant parameter affecting the population of contaminating stars. We explore the effect of Galactic latitude on the performance of our code in Sect. 4.

This simple analysis assumes that stellar dwarf populations are the same in both thin and thick disks. This oversimplification ignores the differences in age and metallicity between the constituents of the thin and thick disks and, therefore, the significant differences that may exist between the stellar dwarf populations within them. Early M-type dwarfs (M0 to M5) have masses above the hydrogen-burning minimum mass, and their luminosity evolves little on time scales up to 10 billion years, whereas brown dwarfs below this limit cool on much faster time scales (Reid 2013). As a result, late M-type dwarfs evolve into later spectral types, and their luminosities drop rapidly over timescales of a Gyr or less. The thick disc, which is older than the thin disc, should, therefore, be depleted of late-type brown dwarfs (M6 to M9 and L), and T dwarfs should be significantly less luminous in the thick disk than in the thin disk (see also the discussion in Caballero et al. 2008). This suggests that the stellar densities reported in Fig. 4 are likely to be seriously overestimated in the thick disk at a given magnitude for spectral types later than M5.

As a conclusion to this analysis, we restrict the modelling of the Galaxy's brown dwarf population to the thin disk and analyse the impact of stellar density through its dependence on Galactic latitude. In the coming years, Euclid and James Webb Space Telescope data will enable a more detailed understanding of the relative populations of brown dwarfs in the thin and thick disks.

We now return to the formulation of our Bayesian model for the description of the stellar dwarf population. The parameters of this population are magnitude (or heliocentric distance), and spectral type $\{H_E, spt\}$. We use the Euclid H_E band as the reference band for calculating magnitudes and the spectral types from M6 to T9. Using the notation described in Sect. 2, we write the weighted evidence of this population as follows:

$$W_s = \sum_{M6}^{T9} \int_{-\infty}^{+\infty} \rho_s^{(l,b)}(H_{mod}, spt) \mathbb{P}(D|H_{mod}, spt) dH_{mod}, \quad (10)$$

where $\rho_s(H_{mod}, spt)$ is the surface density of the contaminating brown dwarf population of Euclid magnitude H_{mod} and spectral type spt , at a given Galactic longitude l and latitude b . We model the spatial distribution across the Galaxy in $\text{mag}^{-1} \times \text{deg}^{-2} \times \text{spt}^{-1}$ units as a function of the heliocentric distance to the star d ,

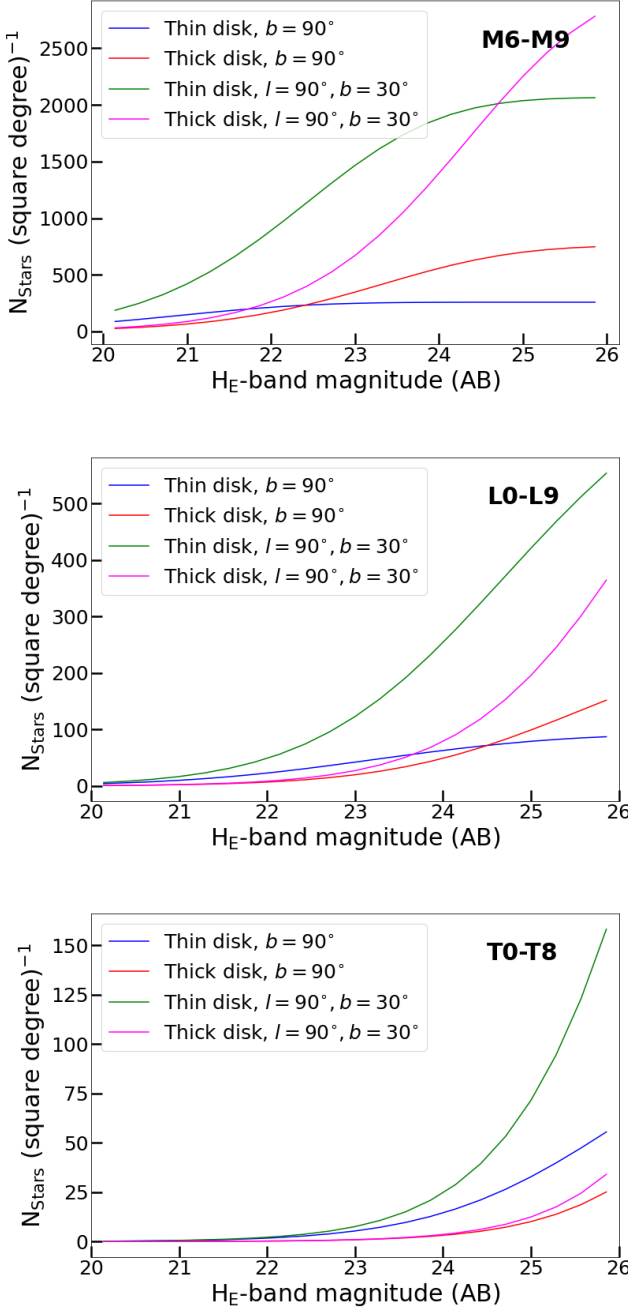


Fig. 4: Brown dwarf number counts as a function of H-band magnitude for the thin and thick discs in two different field locations ($b = 90^\circ$ and $(l, b) = (90^\circ, 30^\circ)$). Top: M6 to M9 spectral types, middle: L0 to L9 and bottom: T0 to T8.

assumed to be far smaller than the solar galactocentric distance R_\odot (Caballero et al. 2008):

$$\rho_s^{(l,b)}(H_{mod}, spt) \approx \rho_{0,spt} \exp\left(\frac{\mp Z_\odot}{h_Z}\right) \mathcal{R}(d_{H_{mod}}, l, b), \quad (11)$$

where,

$$\mathcal{R}(d_{H_{mod}}, l, b) = \exp\left[-d_{H_{mod}} \left(-\frac{\cos(b) \cos(l)}{h_R} \pm \frac{\sin(b)}{h_Z}\right)\right] \quad (12)$$

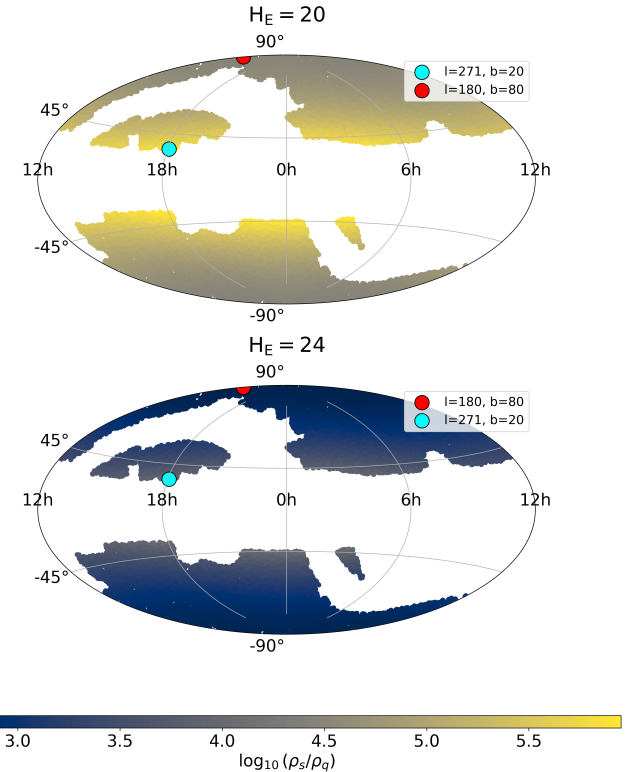


Fig. 5: Ratio of the surface density of brown dwarfs of spectral type M6 to T8 to the surface density of $z > 7$ quasars over the Euclid footprint shown in Galactic coordinates and galactic projection. Top: for magnitude $H_E = 20$, bottom for magnitude $H_E = 24$.

where $\rho_{0,spt} \exp\left(\frac{\mp Z_\odot}{h_Z}\right)$ is the local volume density of brown dwarfs of spectral type spt , Z_\odot the height of the Sun above the Galactic plane (assumed to be 27 pc), h_Z and h_R the scale height and length of the thin disk as mentioned above, and the sign convention indicates whether the source is above or below the Galactic plane (see Caballero et al. 2008). Finally, H_{mod} and $d_{H_{mod}}$ are related through:

$$H_{mod} - M_{H_{mod}} = 5 \log(d_{H_{mod}}) - 4 + 3.09 E(B - V), \quad (13)$$

where H_{mod} and $M_{H_{mod}}$ are the apparent and absolute magnitudes in the reference band H_E and $E(B - V)$ the interstellar reddening.

Using the modelling of the high- z quasar population (Sect. 2.2) and the MLT population described in this section (M6 to T9), we derive the ratio of the brown dwarf to high- z QSO density on the Euclid footprint. This is shown in Fig. 5 for two different apparent magnitudes.

Fig. 6 shows the densities of quasars and M6 to T9 brown dwarfs for two positions with different Galactic coordinates in the Euclid footprint.

2.4. The contaminant galaxy model

There are two different types of galaxies susceptible to contaminating the quasar samples because they display red colours that mimic those of high- z quasars, in particular at low SNR: early-type galaxies at intermediate redshift ($1 < z < 2$) on the one hand, and dusty star-burst galaxies on the other hand. The former exhibit an important 4000Å break because they are dominated by an old stellar population, whereas the presence of dust

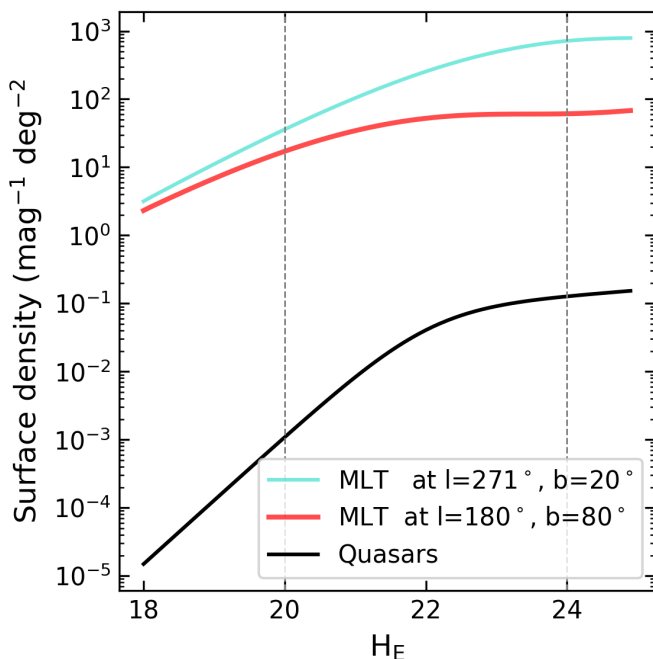


Fig. 6: Surface number densities of MLT stars compared to $z > 7$ quasars, as a function of apparent magnitude, in two different locations of the Euclid footprint.

reddens the latter. To assess the extent of this contamination by intermediate- z galaxies, we have carried out two different tests. The first one consists of precisely determining the contaminant population by using straightforward simulations. The second one is to quantify the contamination in the real Universe based on the COSMOS2022 field (Weaver et al. 2022) by computing the Luminosity Function (LF) of the contaminant population. The LF will be used later to model the abundance of contaminant galaxies.

To precisely identify the contaminant population, we run Owl-z on a simulated catalogue containing 100,000 galaxies uniformly sorted in redshift ($0 \leq z \leq 6$), spectro-photometric templates, and extinction values (between $0 \leq A_V \leq 3$ magnitudes), using the Calzetti extinction law (Calzetti et al. 2000). The simulated catalogue was generated using `make_catalogue`, a tool from the HyperZ tool (Bolzonella et al. 2000). The template library includes two evolutionary synthesis models: a delta burst -Single Stellar Population (SSP)- from the Bruzual & Charlot code (Bruzual & Charlot 2003), with Chabrier IMF (Chabrier 2003) and solar metallicity, and 10 Starbursts99 templates (Leitherer et al. 1999), including emission lines, for single bursts and constant star formation rate models, each one spanning five metallicities ($Z = 0.04, 0.02, 0.008, 0.004$ and 0.001) and 37 ages for the stellar population (between 0 and 1 Gyr). Apparent magnitudes and associated errors have been computed using these templates, sorted to uniformly sample the range of magnitudes where galaxies are expected to be the dominant population in the EWS, in the reference H_E -band, that is $22 \leq H_E \leq 25$. Photometric error bars and noise are scaled to apparent magnitudes, assuming a Gaussian distribution, according to the expected SNR in the different bands used in the EWS. The probability threshold for the selection as a quasar is set to $P_q = 0.1$ for this analysis, following Mortlock et al. 2012 and Euclid Collaboration: Barnett et al. 2019.

The first result of this experiment is that young starbursts, represented by the Starburst99 models, only contaminate the sample at low SNR values for extremely high values of $A_V \geq 1.5$, spanning a relatively broad domain in redshift ($1 \leq z \leq 5$). It is important to acknowledge the significant influence of SNR values in the reference magnitude on our selection process. Indeed, a low SNR in the reference filter H induces a noisy determination of the $J - H$ colour, which in turn leads to a higher degree of confusion in the probability calculation and a greater likelihood of misidentifying high- z quasars. This is a general remark affecting all contaminant galaxies but is particularly important for dusty starbursts. The main contaminants among this population are galaxies at $z \gtrsim 4$ with $A_V \geq 1.5$, and galaxies at $1 \leq z \leq 2$ with $A_V \geq 3$. In the two cases, such extremely reddened galaxies are relatively rare in the real Universe at these redshifts.

Our analysis shows that the main contamination comes from early-type galaxies, represented by SSP models, with ages above 1 Gyr, at intermediate redshifts, $1 < z < 2$. Indeed, the spectral energy distribution of early-type galaxies, such as elliptical and lenticular galaxies, is characterised by an old stellar population, well represented by an initial burst of star formation followed by a rapid decline (see e.g. Ali et al. 2024). Contrary to dusty starbursts, these galaxies are relatively abundant at $1 < z < 2$. For this reason, in the following, we consider that the main contamination comes from early-type galaxies. In this regard, our results are consistent with the assumptions of previous works (e.g. Euclid Collaboration: Barnett et al. 2019). The abundance of these galaxies has been well studied at $z \sim 1.5$, for instance, by Zucca et al. 2006, who studied the evolution of the LF for different filters and spectrophotometric types of galaxies. We can use these previous findings to guide our modelling in the sensitive magnitude domain, as shown below.

After identifying the nature of the contaminant galaxies, we determine the LF of this population. For this need, we use the Euclidised COSMOS2022 catalogue (Weaver et al. 2022), named E-COSMOS hereafter. This catalogue is described in more detail in Sect. 4.3.3. Note that for galaxies detected in the J_E -band at intermediate redshift, the relevant filter for determining the LF is the rest-frame B band.

To represent the LF, we use the classical parameterisation provided by the Schechter function (Schechter 1978) in terms of magnitude given by:

$$n(M) = (0.4 \ln 10) \phi^* [10^{0.4(M^* - M)}]^{\alpha+1} \exp[-10^{0.4(M^* - M)}]. \quad (14)$$

Here, $n(M) dM$ represents the number of galaxies per co-moving Mpc^3 with magnitudes between M and $M + dM$. The parameters are as follows:

- ϕ^* : The normalisation factor, representing the overall volume density of galaxies in $\text{Mpc}^{-3} \times \text{mag}^{-1}$.
- M^* : The characteristic magnitude represents the cut-off between the (bright) luminosity regime dominated by the exponential function and the (faint) regime dominated by the power-law.
- α : The faint-end slope of the luminosity function, describing the distribution of the faintest galaxies.

For the sake of consistency, before selecting the target population of contaminant galaxies in E-COSMOS, we run Owl-z on the E-COSMOS catalogue, with only one contamination source: MLT stars, and the same threshold as before for the selection of high- z quasars. We check the spectrophotometric type and redshift of the 16 galaxies that have been selected as quasars. They are all early-type galaxies at intermediate redshift ($z \sim 1.5$), as expected from previous simulations.

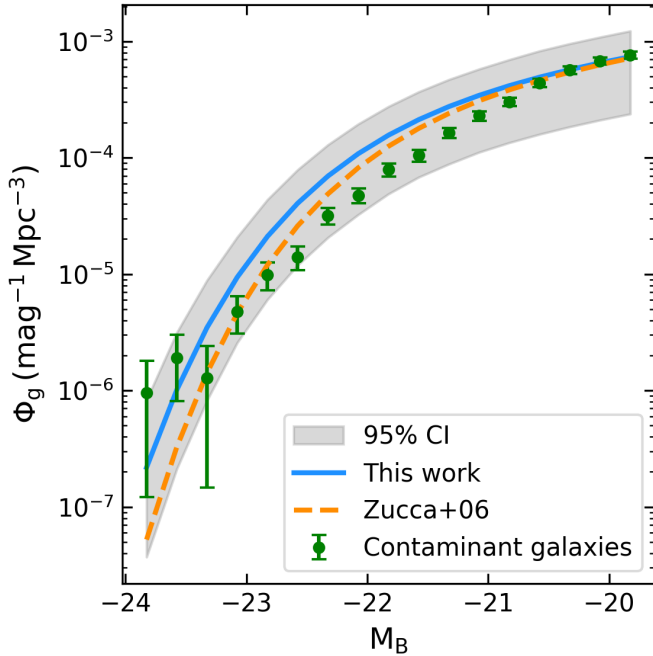


Fig. 7: Luminosity function fit in the B-band (blue) in addition to its 95% confidence interval (grey) for the population of early-type galaxies at $1 < z < 2$ in the E-COSMOS catalogue data (green), compared to the early-type galaxies (dashed orange) luminosity function fit by Zucca et al. 2006.

In order to model the LF for this population of contaminants, we extract from the E-COSMOS catalogue the subset of early-type galaxies within the sensitive redshift domain $1 < z < 2$. To compute absolute magnitudes, we model the spectral energy distribution with a template well suited to represent this population, namely a short, exponentially decaying model with characteristic star-formation time $\tau = 0.1$ Gyr, age = 10 Gyr and solar metallicity ($Z = 0.02$). It is worth mentioning that the precise choice of this model does not change the results. The LF points and their associated error bars are then computed; error bars in the LF include Poisson noise and field-to-field variance. Field-to-field variance is derived using the Trenti & Stiavelli method and calculator (Trenti & Stiavelli 2008). We then fit the data points with the Schechter function in Eq. (14) using a χ^2 minimisation.

Table 2: Comparison of the Schechter function parameters.

	α	M^*	ϕ^* $\times 10^{-4} \text{ Mpc}^{-3}$
Zucca et al. (2006)	-1.23	$-21.5^{+0.48}_{-0.57}$	$3.0^{+1.4}_{-1.2}$
This work	-1.23	$-21.7^{+0.17}_{-0.17}$	$2.9^{+0.6}_{-0.6}$

Notes. Comparison with the results by Zucca et al. (2006) for early-type galaxies at $1 < z < 1.2$. The value of the slope has been fixed to $\alpha = -1.23$ in our fit.

Towards the faint end, we applied a magnitude cut to $M_B < -19.7$ because beyond this limit, our sample suffers from incompleteness. The parameters were chosen to enable easy comparison with the work of Zucca et al. 2006. This motivated us to fix the same value for the parameter α . For comparison, a value of $\alpha = 1.0$ gives a similar result to the function adopted by Euclid

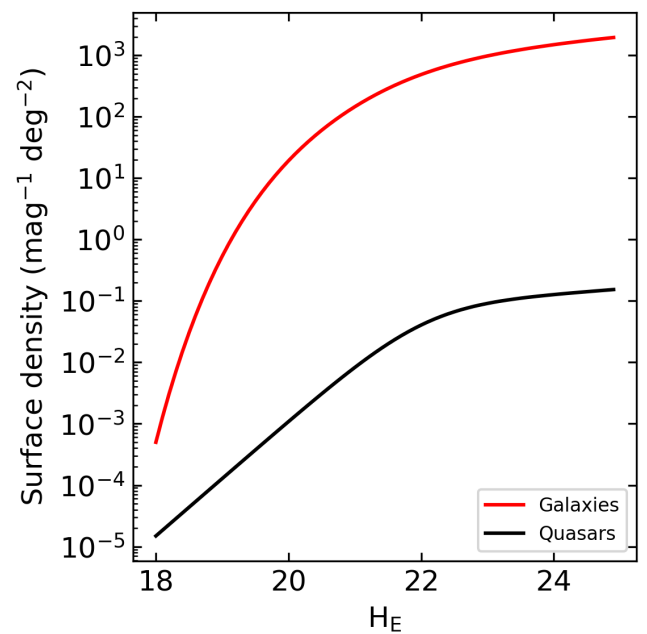


Fig. 8: The surface number density of early-type galaxies integrated in the redshift interval $1 < z < 2$ compared to the quasars surface number density integrated over the redshift interval $7 < z < 12$ quasars, as a function of apparent magnitude.

Collaboration: Barnett et al. 2019 to represent the same population. Note that the precise choice of α is irrelevant here because, on the one hand, only the faintest part of the LF is dominated by the power law and, on the other hand, the population of contaminant galaxies lies preferentially in the bright end.

Fig. 7 shows that our LF points are in good agreement with Zucca et al. 2006. Our fit parameters are shown in Table 2. The LF obtained above is then used to model the prior distribution of early-type galaxies $\rho_{g_i}(H_{\text{mod}}, z)$ given in $\text{mag}^{-1} \times \text{deg}^{-2} \times \text{dz}^{-1}$ units by:

$$\rho_g(H, z_g) = \frac{1}{4\pi} \times \frac{dV_c}{dz_g} \times \Phi_g [H_{\text{mod}} - \mu - K_{\text{corr}}(z_g), z_g], \quad (15)$$

where z_g is the redshift range of the contaminant galaxies $1 < z < 2$ and Φ_g is the luminosity function fit obtained in this work.

For a given set of parameters $\{z_g, H_{\text{mod}}\}$ and an early-type galaxy model g_i , the weighted evidence can be quantified as:

$$W_{g_i} = \int_{-\infty}^{+\infty} \int_{-\infty}^{+\infty} \rho_{g_i}(H_{\text{mod}}, z_g) P(\text{bands}, H_{\text{obs}} | H_{\text{obs}}, g_i) dH_{\text{mod}} dz_g. \quad (16)$$

Fig. 8 displays a comparison between the surface number density of early-type galaxies in the $1 < z < 2$ interval and $z > 7$ quasars as a function of apparent magnitude. The population of contaminant galaxies clearly dominates the number counts.

3. Technical description of Owl-z

The Owl-z code calculates the probability of each preselected candidate belonging to one of the modelled populations, namely high- z quasars, early-type galaxies at intermediate redshifts, and MLT dwarfs. The code is self-contained and written in the Python programming language and its various packages, such as

NumPy, SciPy, and Astropy. It is capable of functioning without any dependencies on external software.

3.1. Inputs

The Owl-z code relies on the computation of colours from the SEDs for all three populations in addition to the K-corrections for quasars and galaxies. To do so, the model requires the filter transmission curve data for each band, as well as a designated reference magnitude. Additional parameters are the magnitude range and the redshift range to explore, for each population. In the case of brown dwarfs, for each spectral type, the range of absolute magnitudes and the local densities should be provided. Templates for each population should be provided, and the code distribution already includes a large number of them for the three populations considered. It is possible to add as many templates as required, provided that they are in the correct format.

3.2. Outputs

The program provides a list of probabilities of belonging to each class for each source. The user then interprets the data and makes a decision by comparing these probabilities with a threshold ζ . Furthermore, it provides a list of useful output parameters, including the optimal redshift for galaxies and quasars and the optimal spectral type for the best-fit stellar model. It also provides the SEDs of the galaxies and quasars that provide the maximum posterior condition. Note that the "best-fit" output of a Bayesian code is the "maximum posterior" (MAP), calculated by maximising the posterior, that is $\max(w_q)$, where $w_q = (w_{q_1}, w_{q_2}, \dots, w_{q_{n_q}})$ are given by

$$w_{q_i} = \rho_{q_i}(H_{\text{mod}}, z) \times P(\mathbf{D}, H_{\text{E}}|H_{\text{E}}, q_i). \quad (17)$$

In the following sections, we use the terms best-fit or MAP, but we always refer to the same Bayesian definition above.

3.3. Efficiency

Owl-z has several efficiency indicators:

- Owl-z requires the user to fill a configuration file which is straightforward to modify, requiring only the input of the user to enable its operation.
- The code is self-sustained, whereby the models and K-corrections are calculated concurrently with the code and the input parameters.
- The code is flexible regarding the numbers and nature of bands used, provided that they do not overlap.
- The code is written with high-performance computing methods in mind and is partly written in Cython for the purpose of enhancing numerical speed.
- In addition to providing a probability value, the model also provides additional output parameters for each source, thus facilitating a more accurate interpretation of the results.

3.4. Limitations

A natural limitation of the code is that the filters correspond to the spectral range of the templates used, for brown dwarfs on the one hand and for galaxies and quasars in the redshift ranges to be explored for each of them.

In the released version of the code corresponding to the one described in this paper, the brown dwarf templates are observed

spectra and cover up to 2500 nm, thus imposing that the filters that can be provided are limited to the K-band. The galaxy and quasar templates have a sufficient spectral range for the redshift ranges explored in this paper and do not impose additional limits.

As will be seen later in this paper, in Sect. 4.2, the colours in the WISE filters have been used to further model the SED beyond the K-band, but this is exclusively possible with the tabulated data provided in Best et al. 2017 and used in the code and cannot be generalised to other datasets extending beyond K-band. Extending the filters that can be used beyond the K-band would require brown dwarf templates with extended spectral ranges that are not readily available.

4. Validation and Performance

4.1. Methodology

This section is dedicated to the validation of Owl-z using two different approaches. The first one consists of re-identifying all the $z > 7$ spectroscopically confirmed quasars available in the literature. To achieve this, Owl-z was configured on a case-by-case basis with the photometric data from which the individual quasars were identified. The second approach relies on simulating different flavours of the EWS catalogues, allowing us to quantitatively evaluate the performance expected for Owl-z based on the measurement of the completeness, a measurement of how many (if any) quasars we misidentify with this process and purity, a measurement enables us to ascertain whether we are still contaminated among the objects identified as quasars by Owl-z. A global performance metric is also introduced, combining both completeness and purity. Performance estimators are important for optimising the selection of high- z quasar candidates with Owl-z, minimising the demand for spectroscopic follow-up and maximising the confirmation rate with a reasonable observational effort.

4.2. Re-identifying known $z > 7$ quasars

We analyse the performance of our code in recovering known and spectroscopically-confirmed quasars at $z > 7$ and selected from near-IR surveys. The versatility of Owl-z allows us to apply it to the different optical and NIR data sets used in the discovery of these quasars. The objective here is to determine if Owl-z is able to identify them as quasars and to compare their spectroscopic redshift with the redshift obtained by the code.

Table 3 lists the quasars used for this analysis, the photometric bands used for their discovery, their measured spectroscopic redshifts, and their reference magnitude.

The photometric data, different for each quasar, include z -band data (z_{DECam}) from DECaLS (Dey et al. 2019), z - and y -band data (z_{PS1} and y_{PS1}) from The Pan-STARRS1 Surveys (Chambers et al. 2016), g -, r -, i -, z - and y -band data (g_{HSC} , r_{HSC} , i_{HSC} , z_{HSC} , y_{HSC}) from Subaru/HSC and Y -, J -, H - and K -band data from UKIDSS (Warren et al. 2007). Data from WISE (Wright et al. 2010) were also used. Given the shallow depth and non-constraining photometry in the W3 and W4 bands, we only use photometric data from the W1 and W2 bands in the following.

The pre-selection methods used to select these quasars were mainly based on colour selection and the identification of strong Lyman breaks ($z - J > 4$) around $\sim 1\mu\text{m}$. An additional criterion was used for the five cases out of eight where WISE photometry was available, consisting of a $W1 - W2 < 0.7$ colour selection enabling the rejection contamination by T-dwarfs (see Fig. 3).

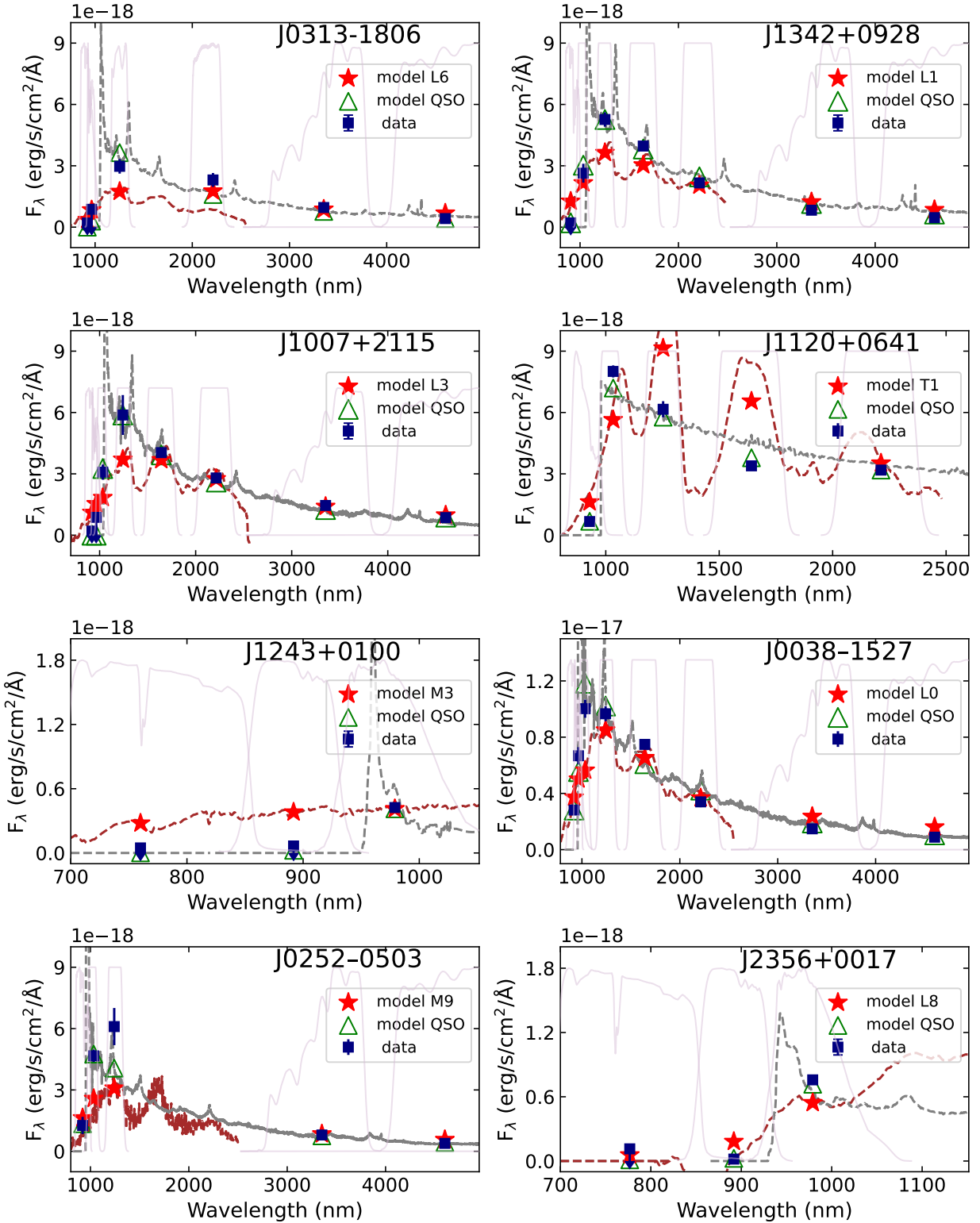


Fig. 9: Photometric data for the eight spectroscopically confirmed quasars at $z > 7$ and the Owl-z best-fit solutions for quasars and MLT dwarfs. The original photometric data points are represented by blue squares. The best-fit quasar model is in dashed grey, the best-fit model for an MLT dwarf is in dashed brown, and the filter transmission curves are shown in solid light purple. Model photometry for best-fit solutions is represented by green triangles for quasars and red stars for MLT dwarfs.

The results of Owl-z are also presented in Table 3, in particular, the output redshifts and P_q values returned by the code. As further discussed in Sect. 4.3.2, the Owl-z output redshifts are in good agreement with the actual redshift of the objects. The pri-

mary potential contaminants expected for the QSOs in this study are L brown dwarfs. Owl-z yields probability $P_q > 0.99$ for all of the QSOs above, showing the high performance of the code in re-identifying the whole sample. Fig. 9 shows the photometric

Table 3: Known quasars at $z > 7$

QSO name	Photometry	z_{spec}	z_{out}	P_q	P_{q2}	mag	Reference
J0313-1806	$z_{PS1}, y_{PS1}, J, K, W1, W2$	7.64	7.7	1	0.25	$y_{PS1} > 23.13$	Wang et al. 2021
J1342+0928	$z_{DECam}, Y, J, H, K, W1, W2$	7.54	7.8	1	0.9	$Y 21.47 \pm 0.19$	Bañados et al. 2018
J1007+2115	$z_{DECam}, y_{PS1}, Y, J, H, K, W1, W2$	7.51	7.65	1	1	$y_{PS1} 21.3 \pm 0.13$	Yang et al. 2020
J1120+0641	z_{DECam}, Y, J, H, K	7.08	7.05	1	-	$Y 19.63 \pm 0.04$	Mortlock et al. 2011
J1243+0100	$g_{HSC}, r_{HSC}, i_{HSC}, z_{HSC}, y_{HSC}$	7.07	6.9	1	-	$y_{HSC} 23.57 \pm 0.08$	Matsuoka et al. 2019b
J0038-1527	$z_{DECam}, y_{PS1}, Y, J, H, K, W1, W2$	7.02	6.95	1	0.9	$y_{PS1} 20.61 \pm 0.1$	Wang et al. 2018
J0252-0503	$z_{DECam}, Y, J, W1, W2$	7.02	6.9	1	10^{-5}	$Y 20.85 \pm 0.07$	Yang et al. 2019
J2356+0017	$i_{HSC}, z_{HSC}, y_{HSC}$	7.01	6.75	1	-	$y_{HSC} 22.94 \pm 0.05$	Matsuoka et al. 2019a

Notes. Spectroscopically confirmed quasars at $z > 7$ with photometric data used for discovery and z_{spec} . Columns z_{out} and P_q are from Owl-z; P_{q2} is given for objects with WISE data.

data, including error bars, for all quasars and the best-fit quasar and MLT dwarf solutions returned by the code.

Some results deserve a specific comment. Owl-z has provided an excellent result for all quasars, including those detected in a single band with non-detection constraints in the others (J2356+0017 and J1243+0100) because the photometric bands in HSC are very deep, and the Ly α break much easier to detect. These quasars have broad Ly α emission and are low-luminosity quasars, matching well the properties of the quasar population model (Sect. 2.2), unlike the SEDs of the MLT dwarfs (Sect. 2.3). As expected, the best-fit MLT solutions for quasars with WISE photometry are late M or L dwarfs, given the aforementioned colour selection criterion ($W1 - W2 < 0.7$) that excludes T dwarfs from photometric selection (Fig. 3).

To assess the impact of WISE data on the performance of Owl-z, we conducted an experiment in which WISE data were removed from the selection process. The results indicate that WISE data were crucial only in identifying one quasar, J0252-0503. Without WISE data, J0252-0503 would have been misclassified as a T star. For the remaining candidates, the exclusion of WISE data primarily led to a decrease in selection probability for the quasar J0313-1806, while the probability for candidates J0038-1527, J1342+0928 and J1007+2115 remained very high (see Table 3).

4.3. Expected performance on EWS simulated data

The performance of Owl-z on the EWS is estimated in terms of completeness and purity in order to ascertain the sensitivity to confusion and contamination by MLT dwarfs and early-type galaxies. To this end, a series of catalogues is simulated in the following sections using Euclid filters (optical I_E and NIR Y_E, J_E, H_E) and sensitivities detailed in Table 4.

4.3.1. Performance: Completeness

To estimate the completeness of the Owl-z selection method, we create a mock catalogue of 500,000 quasars. In order to gain a deeper understanding of the impact of using only Euclid data and of replacing or supplementing the existing data with other bands, three different scenarios have been developed. The first scenario involves using only Euclid data. In the second scenario, the optical band I_E is replaced by the optical z-band of LSST. In the third scenario, in addition to the Euclid optical and NIR data, the photometry is extended to the WISE coverage in the W1 and W2 bands (see Table 5). The sensitivities of these additional bands can also be found in Table 4. The completeness is calculated on the EWS DR6 (Euclid Collaboration: Scaramella

Table 4: Used bands characteristics.

band	λ_{eff}	median SNR	median depth
I_E	6869.74	15.9	26.2
z	8678.90	5	25.9
Y_E	10688.60	6.5	24.3
J_E	13422.62	7.8	24.5
H_E	17410.63	7.2	24.4
W1	33526.00	5	19.8
W2	46028.00	5	18.9

Notes. The Euclid bands characteristics are a duplicate of Table 7 in Euclid Collaboration: Scaramella et al. 2022. The SNR statistics and depths (magnitudes) in the region of interest. All the the statistics have been computed for each channel: optical I_E and LSST z-band and NIR Y_E, J_E, H_E , and WISE channels W1 and W2. The median depth here is evaluated for 5σ point-like source

et al. 2022) footprint, which covers 15,000 deg 2 . Quasars are randomly selected with a flat distribution in redshift in the range $7 \leq z \leq 12$, a flat distribution in absolute magnitude M_{1450} in the range $-29 \leq M_{1450} \leq -22$, a flat distribution over all the SEDs in our library, and finally, a flat spatial distribution within the 15,000 deg 2 of the EWS footprint. For each object in the catalogue, we calculate apparent magnitudes in the Euclid bands, in the LSST z-band, and in the WISE W₁ and W₂ bands. For photometric errors, we adopt those corresponding to the DR1 release of the LSST data (Ivezić et al. 2019) and those for the WISE data; we use the W1 and W2 bands and their corresponding errors from the survey description¹. For Euclid photometric errors, we use the signal-to-noise ratio maps across the EWS footprint as described in Euclid Collaboration: Scaramella et al. 2022; all of this information can be found in Table 4.

Table 5: Scenarios explored in the simulations for the completeness estimation.

Survey	NIR bands	optical bands
Euclid	Y_E, J_E, H_E	I_E
Euclid +LSST	Y_E, J_E, H_E	z
Euclid +WISE	$Y_E, J_E, H_E, W1, W2$	I_E

We define the completeness C of the samples selected by Owl-z as follows:

$$C = \frac{\text{TP}}{\text{TP} + \text{FN}}, \quad (18)$$

¹ wise2.ipac.caltech.edu

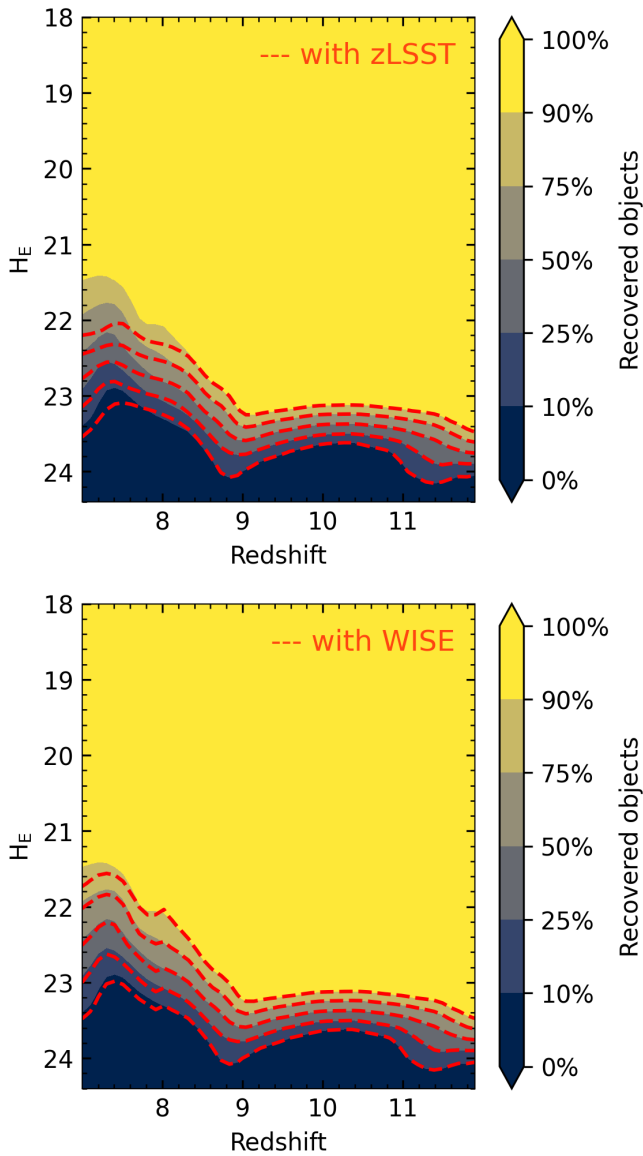


Fig. 10: The selection functions of high redshift quasars determined using *Owl-z* for Euclid $I_E Y_E J_E H_E$ data. The selection function designs the level of completeness per redshift bin; the completeness of a bin is calculated by counting the percentage of quasars in the bin with probability is $P_q > 0.1$. Several cases are shown: (top panel) In red, the optical band O of Euclid is replaced by the z-band from LSST. (bottom panel) Euclid $I_E Y_E J_E H_E$ data and in red Euclid $I_E Y_E J_E H_E$ in addition to WISE (W1 and W2 bands).

where TP (True Positive) is the number of quasars that have been successfully classified as high- z quasars, and FN (False Negatives) is the number of quasars that have been incorrectly classified as contaminants. For the sake of consistency with other work, we define a successful classification when $P_q > 0.1$, and we will examine in Sect. 5 how a different definition affects the results.

For all the objects in our mock quasar catalogue, we calculate the probability P_q , P_s and P_g that the quasar is identified as a quasar, star and galaxy, respectively, as defined in Eq. (1). Ad-

ditionally, the SEDs for each category that allow for a maximum posterior are retrieved.

Results are presented as a function of redshift and H_E magnitude in Fig. 10, for a selection from Euclid's $I_E Y_E J_E H_E$ data. The colours correspond to different increments of the completeness value. We also evaluate how completeness varies when the LSST z-band (top-hand panel in Fig. 10) and the WISE W1 and W2 bands (bottom-hand panel in Fig. 10) are added to the photometric dataset. This is represented by the dotted red contour lines corresponding to the completeness increments.

In addition to the global completeness maps, we show in Fig. 11 the fraction of quasars with $P_q < 0.1$, i.e. quasars misclassified as MLT stars (left panel) or intermediate redshift galaxies (right panel), colour-coded by the percentage of quasars lost in the bin. These maps illustrate the regions of the parameter space where the selection is least complete and help characterise the dominant sources of contamination as a function of redshift and H_E magnitude. As seen in this figure, at $z \sim 7-8$ misclassification as MLT stars dominates, whereas at higher redshifts ($z \geq 8$), the incompleteness reflects the overlap between quasars and mid- z interlopers, increasing with H_E magnitude.

To achieve maximum completeness, quasar magnitudes need to be 2 to 3 magnitudes brighter than the EWS detection limit, depending on the redshift. The closer to the detection limit, and therefore the lower the SNR, the greater the confusion between quasars and brown dwarfs or galaxies at intermediate redshifts, preventing reliable identification.

Between redshift 7 and 8, completeness is lower than at higher redshift, up to $H_E \approx 21$, due to greater confusion with late-type dwarfs. Due to the strong increase in late-type dwarf flux in the reddest part of the optical band and the wide width of the Euclid I_E band, any late-type dwarf will appear significantly fainter in the I_E band than in any z-band image of comparable depth (see Fig. 1). As a result, z-band data from LSST or from the UNIONS survey² provide significantly improved discrimination against L- and T- dwarfs (dashed red curves in the left-hand plot of Fig. 10).

Fig. 10 also shows a loss in completeness around redshift 10 and between magnitudes 22 and 23 of H_E , compared with its value at lower redshift values. We attribute this loss in completeness mainly to an increase in confusion with early-type galaxies as their colours are very similar (see Fig. 12).

Finally, the analysis of completeness, including WISE data (bottom panel in Fig. 10) shows no significant improvement, in contrast to the improvement mentioned in Sect. 4.2 for the re-identification of known quasars at high redshift. Only a modest improvement in the decrease of the confusion with late-type dwarfs is perceptible for the brightest quasars at the lowest redshift. This is due to the fact that the depth of the WISE data (AB magnitude ~ 19 at 5σ in the W1 and W2 bands) does not match that of the Euclid data, making them unconstrained and allowing no significant improvements over the Euclid data alone, either above or below the WISE detection limit.

4.3.2. Redshift estimation

Following Sect. 4.1, the redshift estimated by *Owl-z* corresponds to the maximum posterior value of the parameter z , that is, the maximum posterior $\int W_q(z_{out}, H_E) dH_E$. We refer to it as "photometric redshift" or z_{out} hereafter.

The accuracy of photometric redshift has been estimated by comparing the true redshift injected in the simulation z_{true} to

² <https://www.skysurvey.cc/>

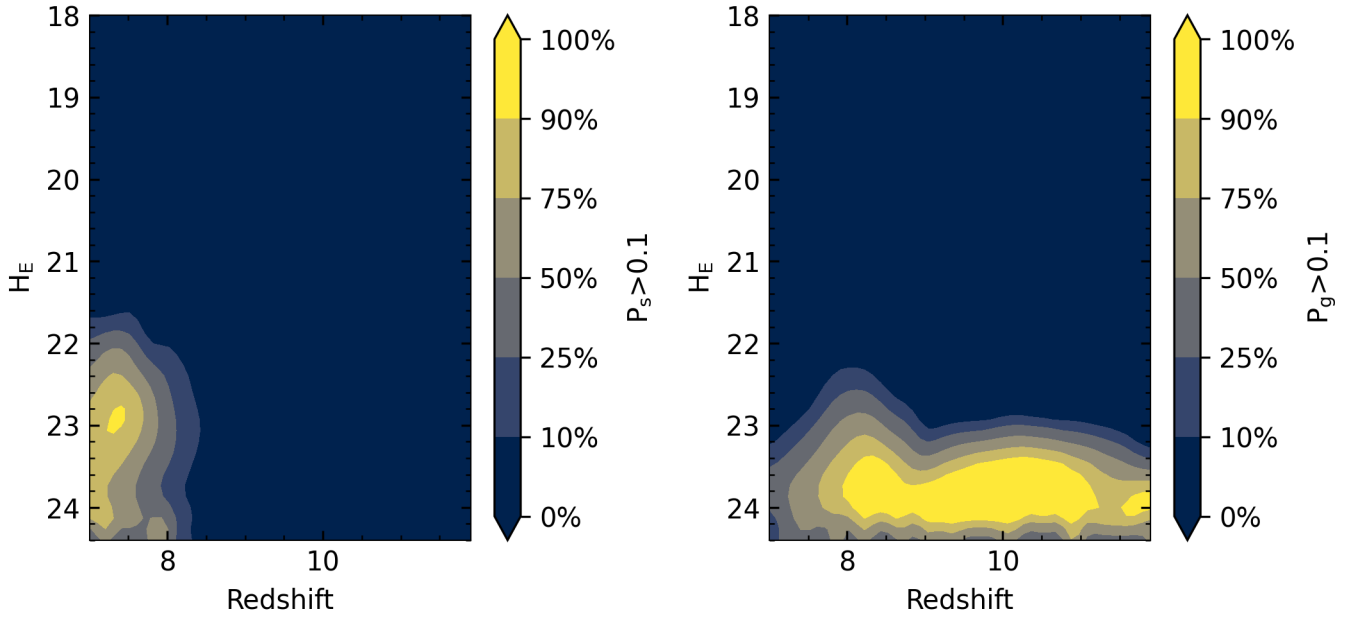


Fig. 11: Incompleteness maps of high- z quasar selection using Owl-z, shown as a function of redshift and H_E -band magnitude. Each panel displays the fraction of quasars with $P_q < 0.1$, i.e. quasars misclassified as MLT stars (left panel) or intermediate redshift galaxies (right panel), colour-coded by the percentage of quasars lost in the bin. These maps illustrate the regions of the parameter space where the selection is least complete and help characterise the dominant sources of contamination.

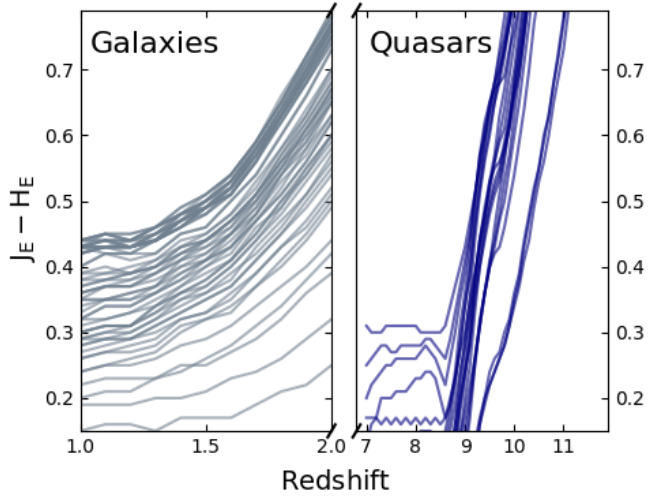


Fig. 12: Tracks of $J_E - H_E$ colours as a function of redshift of Early-Type galaxies (left panel) and high redshift quasars (right panel). For the early-type galaxies, the lower in colour the track is the younger the galaxy.

z_{out} . Fig. 13 displays this comparison for the redshift interval explored in the simulations presented in Sect. 4.3.1. To evaluate the accuracy of the photometric redshift, the sample has been limited to objects brighter than $H_E < 24$, identified as quasars using the same criterion as in Sect. 4.3.1, that is $P_q > 0.1$.

As shown in Fig. 13, an excellent correlation between z_{true} and z_{out} is found, irrespective of the photometric dataset. For the $I_E Y_E J_E H_E$ filter set, the Pearson correlation coefficient is found to be 0.97, whereas the Spearman correlation coefficient is

0.98, indicating a strong linear correlation. The same results are found for the $z Y_E J_E H_E$ dataset. The classical quality estimators used for photometric redshift yield the following results, with $\Delta z = z_{out} - z_{true}$: $\sigma(\Delta z/(1+z)) = 0.030$, the median of $(\Delta z/(1+z)) = -0.007$, and the normalised median absolute deviation, which is less sensitive to outliers: $\sigma_{z,MAD} = 1.48 \times \text{median}(|\Delta z|/(1+z)) = 0.021$. Regarding the fraction of outliers, defined in a conservative way as sources with $\Delta z > 0.1(1+z_{true})$, it is found to be only 2.45% (2.23%) for the $I_E Y_E J_E H_E (z Y_E J_E H_E)$ datasets. Only 13.7% (13.3%) of the sample exhibit $|\Delta z| > 0.05(1+z_{true})$ for the $I_E Y_E J_E H_E (z Y_E J_E H_E)$ datasets.

These results demonstrate the quality and the reliability of the photometric redshift obtained by Owl-z for sources identified as high- z quasars. This is of utmost importance, given the use expected for the output redshift in the selection of samples for spectroscopic follow-up. It is also important in the determination of the purity, as shown in Sect. 4.3.3.

4.3.3. Purity

The purity of the sample expresses the expected reliability of Owl-z in extracting true quasars from photometric observations of real fields, which is applied to the EWS in this particular case. Here, we use the Euclid bands $I_E Y_E J_E H_E$, the photometric depths and the variable SNR maps of Euclid.

We define the purity as:

$$P = \frac{1 + \text{TP}}{1 + \text{TP} + \text{FP}}, \quad (19)$$

that is, the number of true positive identifications (TP) divided by the total number of quasar identifications (TP + FP), where FP stands for false positives. With the above definition, a purity of 100% can either mean that no object (quasar or contaminant) has been identified as a quasar or all the identified objects are

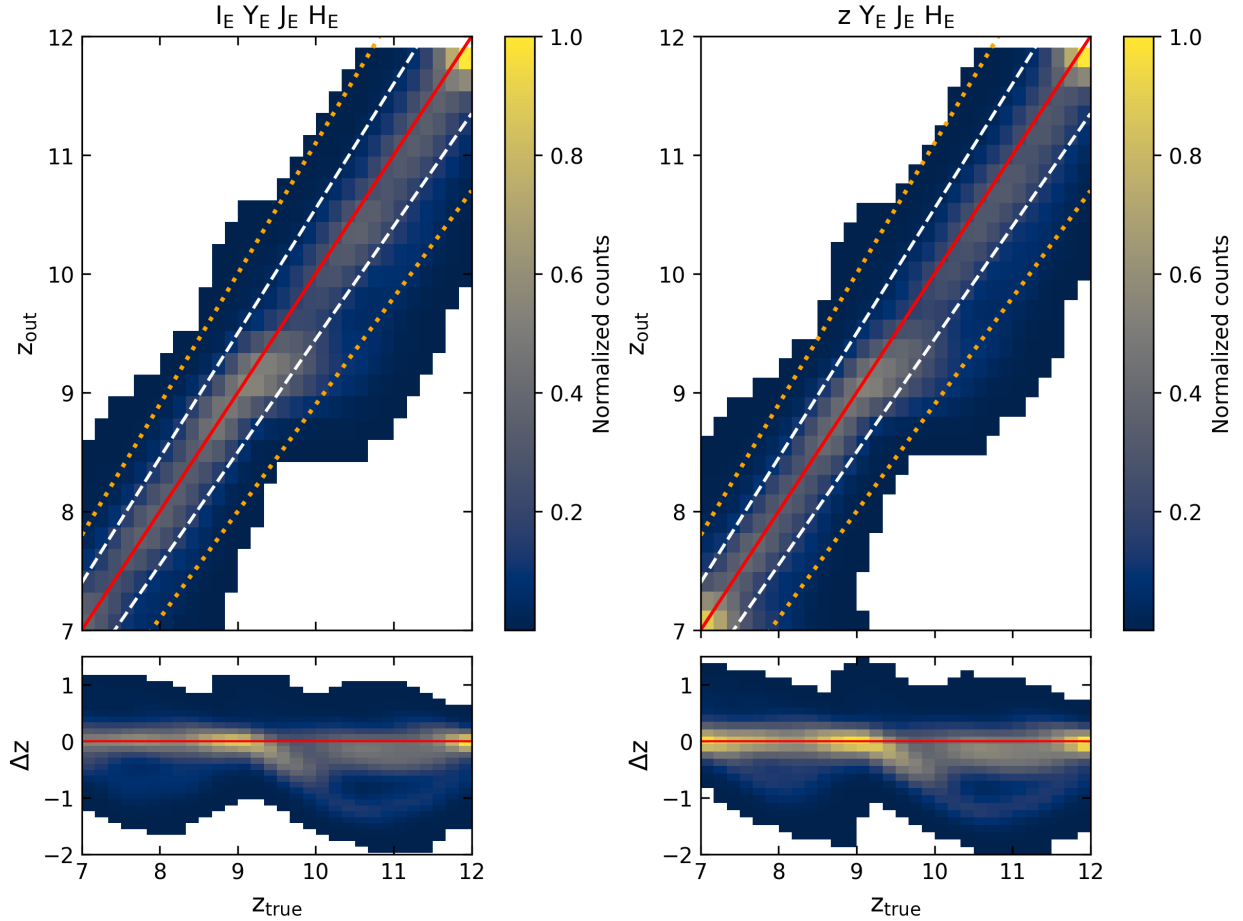


Fig. 13: Top panel shows the comparison between the true redshift and the redshift estimated by Owl-z with both Euclid $I_E Y_E J_E H_E$ dataset (left) and $z Y_E J_E H_E$ dataset (right). Red solid lines display the 1:1 bisector; the thresholds corresponding to $|\Delta z| > 0.1(1+z_{true})$ and $|\Delta z| > 0.05(1+z_{true})$ are also displayed to guide the eye as orange dotted and white dashed lines, respectively. The bottom panel shows the residual $\Delta z = z_{out} - z_{true}$ as a function of redshift, with the red line corresponding to $\Delta z = 0$

quasars. To estimate the purity, we need to simulate as accurately as possible the content of the input photometric catalogues, including the contaminant populations of stars and galaxies in a realistic way. Bright high- z quasars are rare, according to the current LF. For this reason, we force the inclusion of such sources in the simulated catalogues, as explained below, to determine how difficult it will be to identify and study these sources if they ever exist. In order to achieve this, the simulations are conducted on a surface that is 10 times larger than that of the EWS. Subsequently, scaling back to the original surface (1000 deg 2) is performed, whereby only those sources that the LF predicts are accounted for. Note that the definition of the purity as given above accounts for the possible detection of these unique, bright and rare quasars.

The COSMOS2020 field (Weaver et al. 2022) represents an ideal base for this exercise, given the extended wavelength coverage and the exceptionally good quality of the photometric redshifts that can be used as spectroscopic redshifts for our needs. All sources in this field have been fitted using LePHARE (Arnouts & Ilbert 2011) and a library of reference templates, and this provided us with a best-fit template and a redshift. We use these results to compute the Euclid Optical and NIR photometry via a process we call "Euclidisation" (additional details will be provided in Euclid preparation, EC & Garnett et al.). This process has also allowed us to simulate the SNR and associated

photometric errors in each filter. This new Euclid-like COSMOS catalogue will be called hereafter E-COSMOS.

The original COSMOS catalogue covers 2 deg 2 . To cover a statistically significant field of view, multiple realisations of the parent E-COSMOS catalogue are needed. This is done by randomly sorting the coordinates of the field centre within the EWS footprint in such a way that a full (not overlapping) large catalogue is created. This catalogue covers 1000 deg 2 separated into six different areas. The rationale behind this choice is that it represents the smallest surface area over which we can account for a sufficient number of quasars. Furthermore, this surface has been divided across the region of interest in order to accommodate the various scenarios in galactic latitude/longitude, as well as to account for the inevitable differences in resolution, however slight they may be. Fig. 14 and Table 6 display the location of these areas around the Euclid Footprint. It is worth noting that the location of the field is expected to have a direct impact on the performance, given the different distribution of contaminant stars on the one hand and the different SNR achieved across the EWS due to zodiacal light variations on the other hand (Euclid Collaboration: Scaramella et al. 2022). These effects are discussed below. The E-COSMOS catalogue has been cleansed of all stellar objects and is situated at a considerable distance from the Galactic plane. To properly account for the presence of contaminant stars, we randomly inject additional MLT dwarfs into the catalogues,

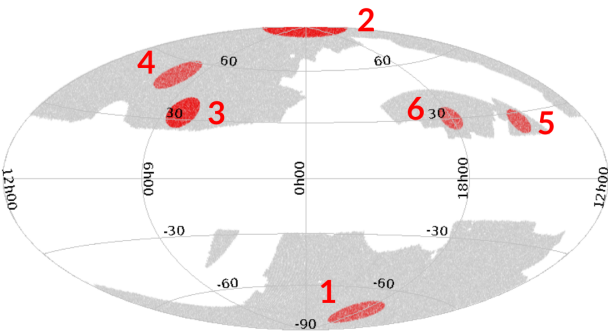


Fig. 14: (red) The location of the regions of focus used in the computation of the purity how in Galactic coordinates and galactic projection. Details on these surfaces can be found in Table 6. (grey) the EWS DR6 footprint.

following the distribution presented in Sect. 2.3, reproducing the number densities expected at the galactic coordinates where the simulated field is located. Since E-COSMOS does not contain any spectroscopically identified high- z quasar, this population has been randomly injected in the simulated fields, following the prescriptions presented in Sect. 4.3.1 to properly account for the SNR in the EWS. High- z quasars are randomly sorted according to their LF. Obviously, the number of bright $z > 7$ quasars is expected to be very small in the EWS field. In particular, the current LF does not predict any quasar brighter than $M_{1450} < -23$ in the entire field. For these rare bright objects, if they exist, we force the measurement of the purity as explained above. To better capture this population, 10 realisations of the entire Euclid footprint are performed, allowing us to retrieve some quasars towards the brightest luminosities and up to redshifts $z > 10$. However, in order to facilitate consistent comparison of the statistical performance estimators C and P , it is necessary to normalise all populations to the same surface area (15,000 deg 2).

Owl-z has been run on these simulated catalogues. The pre-selection criteria and $P_q > 0.1$ threshold applied are identical to those used for the completeness in Sect. 4.3.1. We study the variation of the purity as a function of redshift (z_{out}) and apparent magnitude in the reference filter. The results presented in Fig. 15 provide a summary of the performance of Owl-z in terms of completeness and purity. In each bin, the figure displays the values of C and P . Additionally, it illustrates another performance estimator, the F -measure, which will be defined in Sect. 4.3.4. As shown in this figure, the code is expected to achieve a high purity for the brightest sources, irrespective of the redshift. The influence of the precise choice for the threshold in P_q is discussed in Sect. 5.1.

4.3.4. Global performance

In order to evaluate the global performance of Owl-z by combining both the completeness and purity measurements, we introduce the F -measure as follows:

$$F = 2 \frac{CP}{C + P}, \quad (20)$$

where P is the purity and C is the completeness, according to the definitions in Sect. 4.3.1 and Sect. 4.3.3 respectively. The F -measure is a statistical measurement employed to assess the performance of a classifier (Baeza-Yates & Ribeiro-Neto 2011).

The classification performance—specifically, the code's ability to identify high- z quasars—is evaluated using the F -measure, which indicates the quality of the classification. A higher F -measure indicates a superior classification performance. We use F -measure hereafter as a performance metric.

The results summarising the performance of Owl-z in terms of F -measure are also provided in Fig. 15. As shown in this figure, high values of F -measure are obtained for bright ($H_E < 21$) sources at all redshifts between $7 < z < 11$, indicating that the performance in the spectroscopic confirmation of bright rare quasars is expected to be high. On the contrary, the F -measure drops significantly towards fainter magnitudes and high redshifts, following the drop in the purity value. Note that satisfying results can still be achieved for $H_E < 23$ and $z < 8$. Also, the performance depends on the choice of the probability threshold, hereafter referred to as ζ , as discussed in Sect. 5.1.

To illustrate the effects of contamination, we show in Fig. 17 the contamination by galaxies (background colour) and indicate the relative fractions I_g of galaxies and I_s of MLT stars among the contaminant population. Contamination is almost entirely dominated by galaxies, except in one redshift and magnitude bin where MLT stars also contribute. This is explained by the fact that the colours of MLT stars mainly contaminate the colours of quasars in the redshift bin [7-8] (see Fig. 1), and that the number of contaminants at high magnitudes are dominated by galaxies (see figures 5 and 8).

5. Discussion

In this section, we study the influence of different parameters on the performance of Owl-z, such as the threshold used to select quasars as a function of redshift and magnitude. We also give some guidelines to optimise the selection of high- z quasars and their spectroscopic follow-up. The discussion in this section is based on the performance expected on the EWS.

5.1. Influence of the selection threshold

In the previous section, we consider an object as a quasar candidate when the posterior probability \mathbb{P} is above the threshold $\zeta = 0.1$. This parameter clearly impacts the performance because lower values will improve the completeness while inducing worse purity values and vice-versa. There is a trade-off to find to optimise the performance. Here, we discuss the influence of ζ on F -measure.

To this end, we use the data discussed in Sect. 4.3.3, change the value of ζ to select quasar candidates and recalculate the F -measure in each bin. The results are presented in Fig. 15 for $\zeta = 0.1$ and in Fig. 16 for $\zeta = 0.9$.

Two main trends are observed for sources respectively brighter/fainter than $H_E = 22$.

Increasing the threshold improves purity, albeit at the expense of completeness for faint sources ($H_E > 22$). For bright sources ($H_E < 22$), the completeness is almost unaffected by increasing the classification threshold, thanks to the ability of the code to compute high P_q values for bright quasars.

For faint sources, the performance of Owl-z drops rapidly towards the faintest magnitudes above $H_E = 22$, irrespective of the redshift bin and ζ due to low SNR values, which contribute to a rapid decrease in purity, even when completeness is still good. The analysis of the results shows that early-type galaxies are the main contributors to contamination at these faint magnitudes ($H_E > 22$). Conversely, at bright magnitudes ($H_E < 22$ and

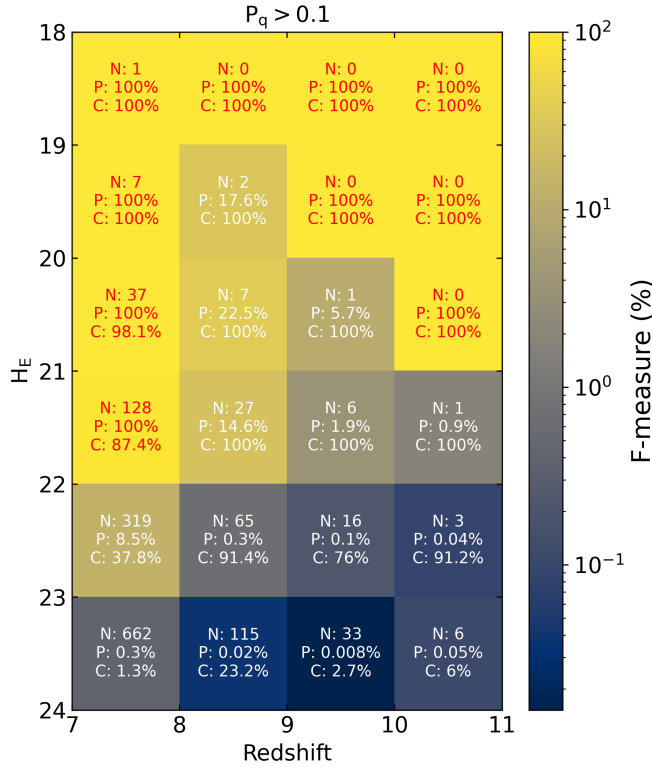


Fig. 15: Classification performance of Owl-z determined using the threshold $\zeta = 0.1$, in each magnitude and redshift bin, N is the number of quasars in the bin, P is the purity, and C is the completeness. The colour code indicates the performance measurement F -measure in each bin

brighter), the SNR is high and enables adequate classification between stars, galaxies and quasars with good completeness, and higher values of ζ improve the purity and the values of the F -measure increase.

In Fig. 15, the $8 < z < 10$ redshift bins for bright candidates ($19 < H_E < 22$) are clearly affected by low purity values. The main sources of contamination in this area are early-type galaxies at redshifts $1 < z < 2$ due to the confusion between the 4000 Å break at intermediate redshift and the Lyman- α break at high redshift, as explained in Sect. 2.4. There is also a minor contribution from contamination by late L-type dwarfs. Increasing the classification threshold has the immediate effect of reducing this contamination and, therefore, improving the purity. As completeness remains high, this results in a significant improvement in F -measure values.

This analysis suggests that an adaptive threshold can be used to optimise the F -measure values in the magnitude/redshift parameter space.

5.2. Optimising the identification of $z > 7$ quasars

We now investigate if the value of the F -measure can be further increased by adjusting the selection threshold ζ in each redshift and magnitude bin. To this end, we use the data discussed in Sect. 4.2, change the value of ζ in increments of 0.1 and select the value that maximises F in each bin. The result is summarised in Fig. 18, showing the value of ζ that maximises F in each bin of magnitude H_E and redshift z_{out} . The results show that, for bright magnitudes ($H_E < 21$), a low threshold value $\zeta = 0.1$ is

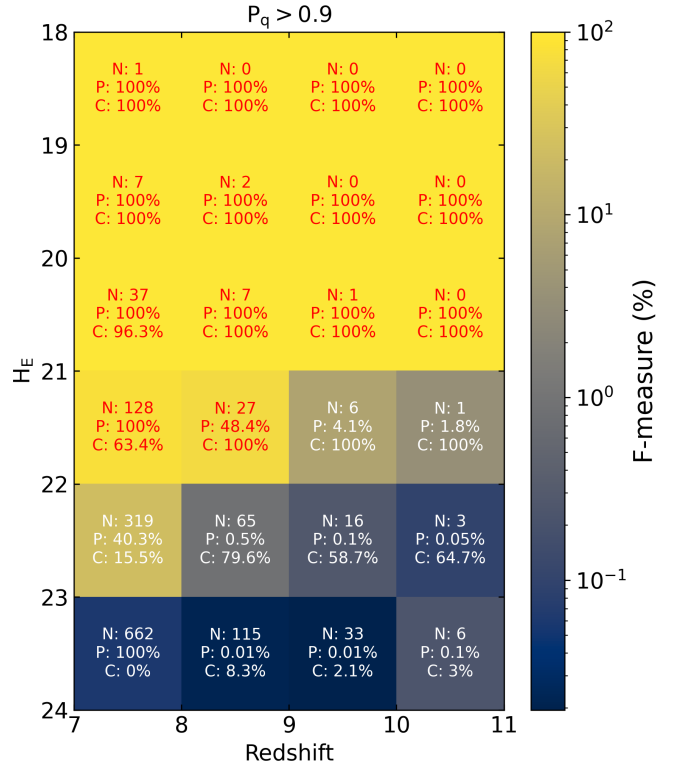


Fig. 16: Classification performance of Owl-z determined using the threshold $\zeta = 0.9$, in each bin we report N : the number of quasars injected in the bin, P : the purity and C : the completeness. The colour code indicates the performance measurement F -measure in each bin.

sufficient to maximise F -measure. This is due to the robustness of the selection for high SNR values irrespective of the redshift, as shown previously. On the contrary, for faint magnitudes ($H_E > 21$), the value of ζ needs to be increased to compensate for the decline in purity, requiring ζ values as high as 0.9 towards the faintest magnitudes.

In conclusion, adopting a variable threshold enables the optimisation of the F -measure and, consequently, the effectiveness of photometric and spectroscopic follow-up campaigns based on Owl-z selected candidates. Finding the best threshold value ζ for a quasar candidate with magnitude H_E and a redshift z_{out} from any other survey data can be done by following the same prescription presented in this article in the case of EWS.

5.3. Influence of the position in the EWS footprint

In this section, we evaluate the effect of different locations in the EWS footprint. As described in [Euclid Collaboration: Scaramella et al. 2022](#), different zodiacal light levels across the footprint modify the SNR for a given magnitude in each filter, and different sky positions and Galactic coordinates introduce varying stellar densities, as described in Sect. 2.3. To this end, we select six different regions in the Euclid footprint, representative of different zodiacal light levels and Galactic coordinates. These regions are shown in Fig. 14, and Table 6 lists their Galactic coordinates and SNR values at reference magnitudes in all Euclid filters.

According to the results presented in Sect. 4, the confusion by MLT dwarfs is only sensible in the redshift interval $z = [7, 8]$,

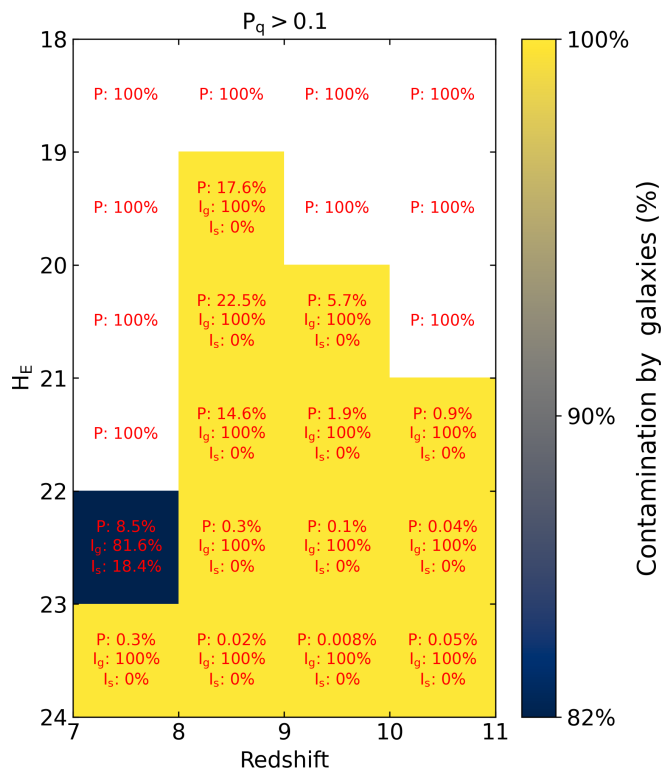


Fig. 17: Contamination by galaxies indicated by the colour map for the same quasar selection parameters as in Figure 15. The overlaid text indicates the purity of the quasars as in Figure 15 and the relative fractions of contamination by galaxies (I_g) and MLT stars (I_s).

where there is also contamination by early-type galaxies. Therefore, we focus the analysis on this redshift bin because it is more susceptible to being affected by the precise distribution assumed for MLT stars. In addition, this redshift bin is also the most populated by quasars, meaning that the results are expected to be statistically more significant than in the other bins. For each one of these regions, we compute simulated catalogues following the prescriptions in Sect. 4.3.3, and we run Owl-z to derive the value of F -measure.

The results are shown in Fig. 19 and display minor variations in the values of F -measure. Regions 5 and 6 exhibit a slight decline in F -measure within the magnitude bin [21, 22] compared to the others. This can be attributed either to the fact that these regions possess the lowest Galactic latitudes ($b = 26$ and $b = 30$) or to the most unfavourable SNR values. According to the results presented in Sect. 4, the comparison with region 3, which is also at a low Galactic latitude but has higher SNR values, suggests that SNR variation is the dominant factor in variations in F -measure. In other words, brown dwarf contamination does not appear to depend significantly on Galactic latitude within the Euclid footprint, which is consistent with figure 4 and with the fact that up to magnitude ≈ 22 contamination is dominated by late-type L and T dwarfs at distances small compared to the scale height of the Galactic disc.

5.4. Influence of thick disk MLT

We aim to evaluate the robustness of our selection process when adding contamination by thick disk MLTs that are not included

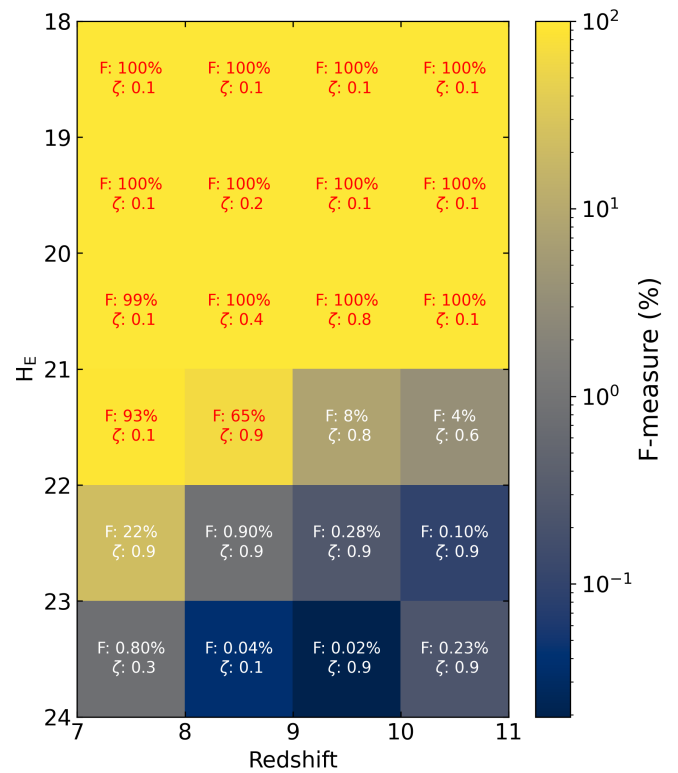


Fig. 18: Classification performance of Owl-z on the magnitude H_E and redshift z_{out} plane. The threshold value of ζ that maximises F -measure is given for each bin.

in the model. We evaluate the impact on the F -measure of adding a contribution of thick-disk brown dwarfs to the input catalogue, following the prescriptions described in section 4.3, and ignoring differences in brown dwarf populations between the thin and thick disks. To do so, we employ the density function outlined in Sect. 2 to generate a population of MLT dwarfs from the thick disc, in addition to the previously added MLT dwarfs from the thin disc, and we analyse the impact on F -measure on the six regions introduced previously. The results are presented in Fig. 20, comparing two scenarios: one where only thin disk MLT dwarfs are injected in the input catalogue (shown by yellow lines) and another where thick disk MLT dwarfs are added (shown by blue lines). The trends on these graphs can be qualitatively explained by the relative density of stars between the thin and thick disks as a function of magnitude. At low magnitudes, the thin disk dominates at all Galactic latitudes, and there are no differences between the two scenarios. At magnitudes above 21, however, and at high Galactic latitudes only (see figure 4), the thick disk population begins to contribute to the counts and introduce a difference between the two scenarios (regions 1, 2, 4 and to a lesser extent region 3, which is at a relatively low Galactic latitude but closest to the Galactic centre in longitude). Overall, this analysis serves as a sanity check in confirming that the precise modelling of the thick disk is unlikely to significantly affect the results for the EWS, but would be warranted for deeper surveys.

Fig. 20 illustrates the drop in F -measure as more contaminants are introduced to the examined catalogues. These added contaminants are MLT stars drawn from the thick disk population, and have been introduced into all catalogues, including Regions 2 and 1, which are the furthest from the Galactic plane. The Bayesian model cannot predict such MLT stars far from the

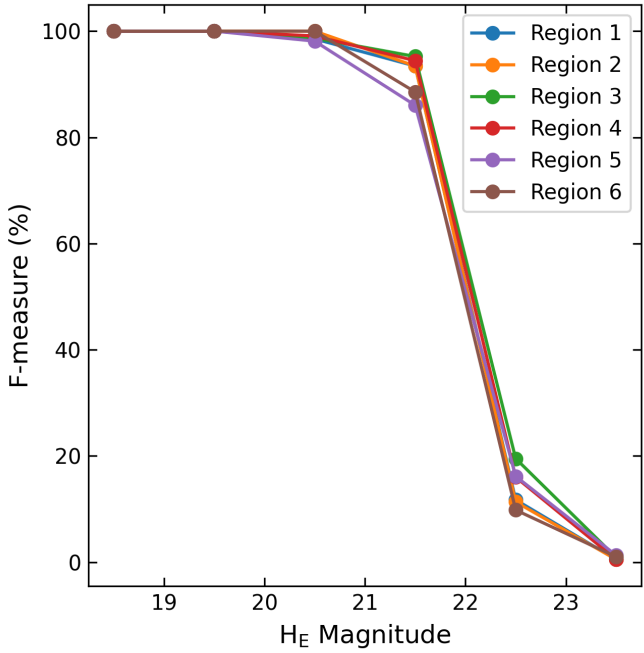


Fig. 19: F -measure evolution as a function of the H_E magnitude in each of the regions shown in Table 6, computed in the $7 < z < 8$ interval.

galactic plane, as it only includes thin disk modelling (see section 2.3). In Regions 5 and 6, which are the closest to the Galactic plane, the Bayesian model expects a high number of contamination from MLT. Consequently, Owl-z does not classify MLT resembling QSO as QSO. However, when we move farther from the Galactic plane (Regions 1, 2, and 4), additional contaminants that the model does not expect are encountered. As a result, they are more likely to be misclassified as a QSO, which in turn lowers the accuracy, i.e. the F -measure of the Owl-z classification.

5.5. Comparison with previous works

The results obtained in this article can be compared to previous similar works, at least qualitatively. A proper comparison will need to run the various codes on the same simulated catalogues, which is currently impossible because not all codes are publicly available. The Bayesian classification approach is similar to that adopted by Pipien et al. 2018b for the analysis of the CFHQsIR survey (Pipien et al. 2018a) searching for quasars at $6.5 < z < 7.5$. Our results in the lowest redshift bin are comparable to those of Pipien et al. 2018b. Note that Pipien et al. 2018b do not include the population of contaminant galaxies, a choice that has no impact on their results because the dominant contamination in this bin comes mainly from LT stars, as shown in Sect. 4.

Our work also compares to and complements the study conducted by Euclid Collaboration: Barnett et al. 2019 on the EWS using a similar Bayesian classification method and the same contaminant populations of stars and galaxies. Although these approaches are comparable, our prior models and definitions of contaminant populations differ. Table 7 highlights the differences between the modelling of quasar and contaminant populations in these different studies. With respect to Euclid Collaboration: Barnett et al. 2019, the work with Owl-z extends the study be-

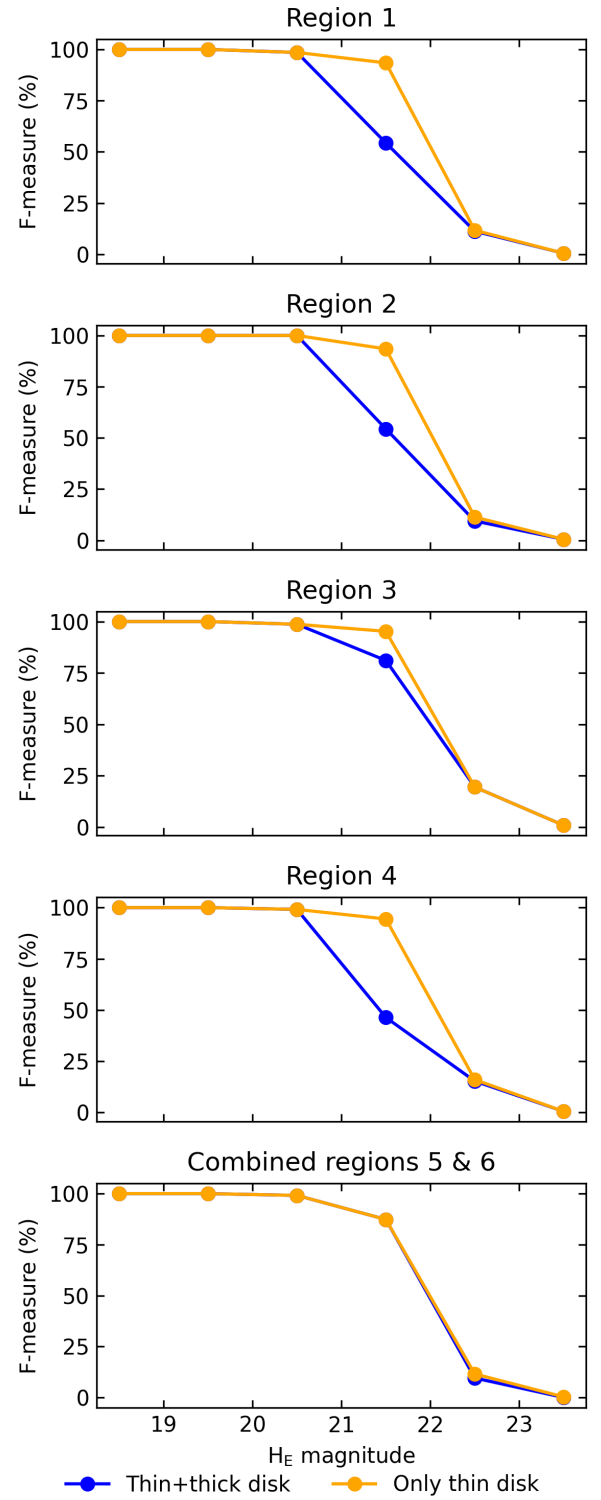


Fig. 20: F -measure evolution as a function of the H_E magnitude in each of the regions shown in Table 6, computed in the $7 < z < 8$ interval. Two cases are shown for the contribution of MLT stars. In yellow is presented the evolution when only the thin disk contribution is accounted for, both in the simulation and the Bayesian modelling. In blue, the same result is shown when the contribution of the thick disk is added to the simulations.

yond $z > 9$, and introduces different performance metrics in addition to the completeness, namely purity and F -measure (com-

Table 6: Properties of simulated areas and catalogues

Notes. Simulations across the EWS footprint use reference magnitudes of 24 for Y_E , J_E , and H_E , and 24.5 for I_E . The SNR values are averaged over each surface.

Region	Surface (deg 2)	l(deg)	b(deg)	SNR $_{I_E}$	SNR $_{Y_E}$	SNR $_{J_E}$	SNR $_{H_E}$
1	200	270	-75	17.5	7.0	8.45	7.9
2	200	180	85	16.5	6.6	7.8	7.4
3	200	78	35	17.8	7.0	8.5	7.7
4	200	107	55	18.6	7.4	8.8	8.22
5	100	227	26	13.8	5.6	6.6	6.1
6	100	270	30	14.3	5.9	7.1	6.5

bining completeness and purity). Our definition of purity has also been adapted to account for rare quasars beyond $z > 9$ that could be found in the EWS if they ever exist. We also use updated prescriptions for the quasar LF and the contaminant populations. It is worth noting that we have used here the EWS SNR maps, making our predictions closer to the real observations. The performance of Owl-z in terms of completeness in the common redshift range with [Euclid Collaboration: Barnett et al. 2019](#) is found to be better than in this previous work. The reason for this improvement is mainly the fact that the global SNR is expected to be better than assumed by [Euclid Collaboration: Barnett et al. 2019](#). On the contrary, the effect of the detailed 2D modelling of the SNR in the EWS has little impact on the performance of Owl-z and similar codes, possibly because the depth is not dramatically different across the survey, as discussed in Sect. 5.3.

Possibly the main advantage of Owl-z with respect to other existing codes is its versatility in adapting to different photometric surveys, as shown in Sect. 4.2. The code will be publicly available and open to access.

6. Conclusions and perspectives

The conclusions of this work can be summarised as follows:

- This work is intended to be the reference article presenting Owl-z, a public Bayesian code aiming at identifying $z > 7$ quasars in massive photometric surveys. Owl-z is based on the classification of sources as high- z quasars or contaminants, the latter being MLT stars or early-type galaxies at intermediate redshifts. The populations of contaminants have been carefully modelled for the needs of the Bayesian model selection. Although the code has been tuned to be used on the EWS, it can be easily adapted to different photometric surveys, as shown in this work.
- Owl-z has been able to re-identify all spectroscopically-confirmed quasars at $z > 7$. This exercise has also demonstrated the versatility of Owl-z regarding its application to different photometric catalogues.
- The performance of Owl-z based on F -measure, a metric combining completeness and purity, has been estimated using simulations for the EWS in a wide range of redshifts ($7 < z < 12$) and reference magnitudes ($18 < H_E < 24.5$). The results show that Owl-z reaches full performance for bright sources ($H_E < 22$) irrespective of the redshift, meaning that the performance in the spectroscopic confirmation of bright rare quasars selected by Owl-z is expected to be high. The performance drops significantly towards fainter magnitudes and high redshifts.
- The threshold value for the selection of quasars can be applied in the post-treatment phase, meaning that this value can be tuned to optimise the selection of $z > 7$ quasars.

For instance, a small/large value can be used for the brightest/faintest sources ($H_E < 21$ and > 21 , respectively) to optimise the performance. Given the steep change of the optimum threshold on the magnitude versus redshift plane, a relatively crude cut on this plane could be adopted to optimise the spectroscopic follow-up.

- A uniform performance is obtained with Owl-z across the EWS footprint, irrespective of the Galactic coordinates and relative SNR values.
- The results of the code remain robust despite inevitable uncertainties in the detailed modelling of the contaminating stellar populations, in particular, the thin and thick disks.

The results obtained with Owl-z are promising and demonstrate its value as a flexible and robust tool for high- z quasar selection. However, several avenues can be explored to enhance its capabilities further and expand its applicability to upcoming large photometric surveys. These perspectives span both methodological improvements and broader scientific applications.

One major development direction involves extending Owl-z to additional photometric datasets, including those from LSST, Roman, and JWST. While the current implementation is tailored to Euclid-like data, its Bayesian framework is inherently adaptable. Nonetheless, brown dwarf spectral templates used in the model become unreliable beyond the K-band, highlighting the need to incorporate theoretical templates or real spectra from complementary instruments to maintain performance across varying wavelength ranges.

Integrating machine learning techniques into the classification pipeline offers another exciting prospect. Deep learning models, such as convolutional neural networks, could be used with Owl-z to refine candidate selection and optimise the balance between completeness and purity. This hybrid approach may prove especially effective at fainter magnitudes, where the performance of Owl-z currently diminishes.

In addition to the photometric selection methods employed in this study, the potential for utilising morphological information in classifying sources presents an intriguing avenue for future research. Incorporating morphological data could differentiate extended sources, such as early-type galaxies, from point sources like high- z quasars. This classification, however, is contingent upon factors such as redshift and magnitude, as higher and elliptical redshift galaxies may appear increasingly compact due to resolution limits. While this work does not include morphological analysis due to its complexity and the technical challenges associated with modelling Euclid detections of extended objects, we acknowledge that such an approach could significantly enhance the quasar selection process. Future studies could explore this integration, potentially refining our ability to mitigate contamination from non-quasar sources and improving detection efficiency in the search for high- z quasars.

Additionally, improved modelling of contaminant populations is vital for maintaining selection accuracy in deeper surveys. Future work should consider a broader range of contaminants, including dusty star-forming galaxies, transients, and thick-disk brown dwarfs. These populations will likely become more prominent as surveys probe deeper into the high- z Universe.

`Owl-z` would also benefit from being embedded within a broader observational framework, including dedicated spectroscopic follow-up strategies. Systematic spectroscopic validation of candidates would refine the Bayesian thresholds and inform better post-selection filtering.

From a practical standpoint, future developments should also include optimising photometric preselection criteria to better handle systematic uncertainties and noise. This may involve simulation-based studies to understand the code's response to varying observational conditions and tune selection thresholds accordingly.

Moreover, cross-matching with multi-wavelength surveys (e.g. JWST, ground-based NIR observations) would add confidence to the classification of candidates and help eliminate artefacts or ambiguous detections.

Finally, although `Owl-z` was not originally designed for precise photometric redshift estimation, its outputs show potential in this area. Coupling `Owl-z` with dedicated redshift estimation tools in the post-processing stage could provide more accurate redshift predictions, further enriching its scientific utility.

Acknowledgements. This work makes use of publicly available data from the Euclid mission. We are grateful to members of the Euclid Science Working Group Primeval Universe, and in particular the Quasar Work Package, for their informal feedback and discussions during the development of this study. We would like to extend special thanks to Eduardo Bañados and Daniel Mortlock for their insightful input and collaboration. This research has also benefited from the use of quasar templates provided by Paul Hewett. We acknowledge Yōsuke Matsuoka, Feige Wang, and Jinyi Yang for kindly sharing spectra of quasars at $z > 7$. This research has made use of the Spanish Virtual Observatory project (<https://svo.cab.inta-csic.es>), funded by MCIN/AEI/10.13039/501100011033 through grant PID2020-112949GB-I00, particularly the SpeX Prism Library of brown dwarf spectral templates. We also acknowledge the use of the SVO Filter Profile Service "Carlos Rodrigo", funded by the same grant. This research has been possible thanks to the computing facilities operated by CeSAM data centre at LAM, Marseille, France. Finally, we acknowledge the use of several open-source Python packages, including NumPy, SciPy, Astropy, Matplotlib, and Cython, which were instrumental in our data analysis and performance optimisation.

References

Akeson, R., Armus, L., Bachelet, E., et al. 2019, arXiv e-prints, arXiv:1902.05569

Ali, S. S., De Propris, R., Chung, C., et al. 2024, ApJ, 966, 50

Arnouts, S. & Ilbert, O. 2011, LePHARE: Photometric Analysis for Redshift Estimate, Astrophysics Source Code Library, record ascl:1108.009

Bañados, E., Venemans, B. P., Decarli, R., et al. 2016a, ApJS, 227, 11

Bañados, E., Venemans, B. P., Decarli, R., et al. 2016b, ApJS, 227, 11

Bañados, E., Venemans, B. P., Mazzucchelli, C., et al. 2018, Nature, 553, 473

Bañados, E., Venemans, B. P., Morganson, E., et al. 2014, AJ, 148, 14

Baeza-Yates, R. & Ribeiro-Neto, B. 2011, Modern Information Retrieval the Concepts and Technology Behind Search

Bakos, G. A., Sahu, K. C., & Németh, P. 2002, ApJS, 141, 187

Becker, G. D., Bolton, J. S., Madau, P., et al. 2015, MNRAS, 447, 3402

Belladitta, S., Moretti, A., Caccianiga, A., et al. 2020, A&A, 635, L7

Bennett, J. S., Sijacki, D., Costa, T., Laporte, N., & Witten, C. 2024, MNRAS, 527, 1033

Best, W. M. J., Liu, M. C., Dupuy, T. J., & Magnier, E. A. 2017, ApJ, 843, L4

Bochanski, J. J., Hawley, S. L., Covey, K. R., et al. 2010, AJ, 139, 2679

Bolzonella, M., Miralles, J. M., & Pelló, R. 2000, A&A, 363, 476

Bosman, S. E. I., Davies, F. B., Becker, G. D., et al. 2022, MNRAS, 514, 55

Bovy, J., Hogg, D. W., & Roweis, S. T. 2011, Annals of Applied Statistics, 5, 1657

Bruzual, G. & Charlot, S. 2003, MNRAS, 344, 1000

Burgasser, A. J. 2014, in Astronomical Society of India Conference Series, Vol. 11, Astronomical Society of India Conference Series, 7–16

Burgasser, A. J., Bezanson, R., Labbe, I., et al. 2024, ApJ, 962, 177

Burgasser, A. J. & Splat Development Team. 2017, in Astronomical Society of India Conference Series, Vol. 14, Astronomical Society of India Conference Series, 7–12

Caballero, J. A., Burgasser, A. J., & Klement, R. 2008, A&A, 488, 181

Calzetti, D., Armus, L., Bohlin, R. C., et al. 2000, ApJ, 533, 682

Chabrier, G. 2003, PASP, 115, 763

Chambers, K. C., Magnier, E. A., Metcalfe, N., et al. 2016, arXiv e-prints, arXiv:1612.05560

Dey, A., Schlegel, D. J., Lang, D., et al. 2019, AJ, 157, 168

Dupuy, T. J. & Liu, M. C. 2012, ApJS, 201, 19

Euclid Collaboration, Mellier, Y., Abdurro'uf, et al. 2025, A&A, 697, A1

Euclid Collaboration, Schirmer, M., Jahnke, K., et al. 2022, A&A, 662, A92

Euclid Collaboration: Barnett, R., Warren, S. J., Mortlock, D. J., et al. 2019, A&A, 631, A85

Euclid Collaboration: Scaramella, R., Amiaux, J., Mellier, Y., et al. 2022, A&A, 662, A112

Euclid Collaboration: van Mierlo, S. E., Caputi, K. I., Ashby, M., et al. 2022, A&A, 666, A200

Fan, X., Bañados, E., & Simcoe, R. A. 2023, ARA&A, 61, 373

Fan, X., Strauss, M. A., Becker, R. H., et al. 2006, AJ, 132, 117

Gaia Collaboration, Recio-Blanco, A., Kordopatis, G., et al. 2023, A&A, 674, A38

Hainline, K. N., D'Eugenio, F., Sun, F., et al. 2024a, ApJ, 975, 31

Hainline, K. N., Helton, J. M., Johnson, B. D., et al. 2024b, ApJ, 964, 66

Hogg, D. W., Baldry, I. K., Blanton, M. R., & Eisenstein, D. J. 2002, arXiv e-prints, astro

Ivezić, Ž., Kahn, S. M., Tyson, J. A., et al. 2019, ApJ, 873, 111

Kang, Y., Hennawi, J. F., Schindler, J.-T., Tamanas, J., & Nanni, R. 2024, arXiv e-prints, arXiv:2412.03029

Laureijs, R., Amiaux, J., Arduini, S., et al. 2011, arXiv e-prints, arXiv:1110.3193

Leitherer, C., Schaerer, D., Goldader, J. D., et al. 1999, ApJS, 123, 3

Maiolino, R., Scholtz, J., Curtis-Lake, E., et al. 2024a, A&A, 691, A145

Maiolino, R., Scholtz, J., Witstok, J., et al. 2024b, Nature, 627, 59

Matsuoka, Y., Iwasawa, K., Onoue, M., et al. 2019a, ApJ, 883, 183

Matsuoka, Y., Onoue, M., Iwasawa, K., et al. 2023, ApJ, 949, L42

Matsuoka, Y., Onoue, M., Kashikawa, N., et al. 2019b, ApJ, 872, L2

Mortlock, D. J., Patel, M., Warren, S. J., et al. 2012, MNRAS, 419, 390

Mortlock, D. J., Warren, S. J., Venemans, B. P., et al. 2011, Nature, 474, 616

Nanni, R., Hennawi, J. F., Wang, F., et al. 2022, MNRAS, 515, 3224

Oke, J. B. & Gunn, J. E. 1983, ApJ, 266, 713

Pipien, S., Basa, S., Cuby, J. G., et al. 2018a, A&A, 616, A55

Pipien, S., Cuby, J. G., Basa, S., et al. 2018b, A&A, 617, A127

Reid, I. N. 2013, Brown Dwarfs, ed. T. D. Oswalt & M. A. Barstow (Dordrecht: Springer Netherlands), 337–395

Robert, C. P. 2007, The Bayesian choice: from decision-theoretic foundations to computational implementation, 2nd edn. (Springer)

Ryan, R. E. J. & Reid, I. N. 2016, AJ, 151, 92

Schechter, P. 1978, The luminosity function for galaxies and the clustering of galaxies

Scholtz, J., Witten, C., Laporte, N., et al. 2024, A&A, 687, A283

Skrzypek, N., Warren, S. J., & Faherty, J. K. 2016, A&A, 589, A49

Stern, D., Kirkpatrick, J. D., Allen, L. E., et al. 2007, ApJ, 663, 677

Sysoliatina, K. & Just, A. 2022, A&A, 666, A130

Temple, M. J., Hewett, P. C., & Banerji, M. 2021, MNRAS, 508, 737

Trenti, M. & Stiavelli, M. 2008, ApJ, 676, 767

Übler, H., Maiolino, R., Pérez-González, P. G., et al. 2024, MNRAS, 531, 355

Vieira, K., Carraro, G., Korchagin, V., et al. 2022, ApJ, 932, 28

Vieira, K., Korchagin, V., Carraro, G., & Lutsenko, A. 2023, Galaxies, 11, 77

Wang, F., Yang, J., Fan, X., et al. 2021, ApJ, 907, L1

Wang, F., Yang, J., Fan, X., et al. 2018, ApJ, 869, L9

Warren, S. J., Cross, N. J. G., Dye, S., et al. 2007, arXiv e-prints, astro

Weaver, J. R., Kauffmann, O. B., Ilbert, O., et al. 2022, ApJ Supplement Series, 258, 11

Wenzl, L., Schindler, J.-T., Fan, X., et al. 2021, AJ, 162, 72

Wilkins, S. M., Stanway, E. R., & Bremer, M. N. 2014, MNRAS, 439, 1038

Willott, C. J., Delorme, P., Reylé, C., et al. 2010, AJ, 139, 906

Wright, E. L., Eisenhardt, P. R. M., Mainzer, A. K., et al. 2010, AJ, 140, 1868

Yang, J., Wang, F., Fan, X., et al. 2020, ApJ, 897, L14

Yang, J., Wang, F., Fan, X., et al. 2019, AJ, 157, 236

Zucca, E., Ilbert, O., Bardelli, S., et al. 2006, A&A, 455, 879

¹ Aix Marseille Univ, CNRS, CNES, LAM, Marseille, France

² Aix Marseille Univ, CNRS, I2M, Marseille, France

³ Aix Marseille Univ, CNRS, LIS, Marseille, France

⁴ Canada-France-Hawai'i Telescope, Waimea, Hawai'i

⁵ Université Paris-Saclay, Université Paris Cité, CEA, CNRS, AIM, 91191, Gif-sur-Yvette, France

⁶ Leiden Observatory, Leiden University, P.O. Box 9513, 2300 RA Leiden, The Netherlands

	Models used	Quasar prior	Galaxy prior	MLT stars prior
This work	Quasars, low- z galaxies and MLT stars	Matsuoka et al. 2023	LF fitted on real data	Caballero et al. 2008
Pipien et al. 2018b	Quasars and LT stars	Willott et al. 2010	Not used	Caballero et al. 2008
Mortlock et al. 2012	MLT stars, low z galaxies and MLT stars	Willott et al. 2010	Not used	Power-law number counts in combination with an exponential power-law colour distribution for the reddest stars
Euclid Collaboration: Barnett et al. 2019	MLT stars, low- z galaxies and quasars	Willott et al. 2010	Parametrised function fit to elliptical galaxies	LT stars based on Caballero et al. 2008 and M stars based on Bochanski et al. 2010

Table 7: Comparison of models, priors, and references used in various works.